Rift Focussing and Magmatism During Late-Stage Rifting in Afar, Ethiopia

Chris Moore[1], Tim J. Wright[1], and Andrew Hooper[1]

[1]University of Leeds

November 21, 2022

Abstract

Processes that facilitate the transition between continental rifting and sea-floor spreading remain unclear. Variations in the spatial distribution of extension through Afar and into the Red Sea are indicative of temporal evolution of the rift. We develop a time series of Sentinel-1 interferometric synthetic aperture radar (InSAR) observations of ground deformation covering the whole Afar Rift from 2014-2019, to study the distribution of extension across all magmatic segments. By incorporating GNSS observations, we resolve 3D average velocities in the vertical, rift-perpendicular, and rift-parallel directions. Results show the spatial distribution of long-term plate motions over the rift, as well as deformation at individual volcanic centres, including Dallol, Nabro, and Erta 'Ale. We find that in northern and central Afar, the majority of extension is accommodated within +/- 15-30 km of magmatic spreading centres. In southern Afar, near the Nubia-Arabia-Somalia triple-junction, extension is distributed over 90-180 km, which may indicate an increase in rift focussing with rift maturity. We also observe rapid surface uplift and rift-perpendicular extension at the Dabbahu-Manda-Hararo segment with velocities of 33 +/- 4 mm/yr and 37 +/- 4 mm/yr respectively. These are higher than the background extension rate of 18-20 mm/yr, but have decreased by 55-70 % since 2006-10. The data suggests that this is due to an on-going long-lived response to the 2005-10 rifting episode, with potential continued processes below the segment including a lower-crustal viscous response and magma movement. Continued long-term observations of surface deformation provide key constraints on tectono-magmatic processes in Afar.

Rift Focussing and Magmatism During Late-Stage Rifting in Afar, Ethiopia

C. Moore[1], T. Wright[1], A. Hooper[1]

[1]COMET, School of Earth and Environment, University of Leeds, Leeds, LS2 9JT, UK

Key Points:

- From Sentinel-1 InSAR and GNSS observations, we resolve 3D average surface velocities from 2014-19 across the whole Afar rift
- Rift focusing increases with rift maturity, with distributed extension in southern Afar, and localised extension in north and central Afar
- We observe surface deformation related to magmatism at several volcanic centres including Dallol, Erta 'Ale, Nabro, and Dabbahu-Manda-Hararo

Corresponding author: Chris Moore, ee12cm@leeds.ac.uk

Abstract

Processes that facilitate the transition between continental rifting and sea-floor spreading remain unclear. Variations in the spatial distribution of extension through Afar and into the Red Sea are indicative of temporal evolution of the rift. We develop a time series of Sentinel-1 interferometric synthetic aperture radar (InSAR) observations of ground deformation covering the whole Afar Rift from 2014-2019, to study the distribution of extension across all magmatic segments. By incorporating GNSS observations, we resolve 3D average velocities in the vertical, rift-perpendicular, and rift-parallel directions. Results show the spatial distribution of long-term plate motions over the rift, as well as deformation at individual volcanic centres, including Dallol, Nabro, and Erta 'Ale. We find that in northern and central Afar, the majority of extension is accommodated within $\pm$ 15-30 km of magmatic spreading centres. In southern Afar, near the Nubia-Arabia-Somalia triple-junction, extension is distributed over 90-180 km, which may indicate an increase in rift focussing with rift maturity. We also observe rapid surface uplift and rift-perpendicular extension at the Dabbahu-Manda-Hararo segment with velocities of 33 $\pm$ 4 mm/yr and 37 $\pm$ 4 mm/yr respectively. These are higher than the background extension rate of 18-20 mm/yr, but have decreased by 55-70 % since 2006-10. The data suggests that this is due to an on-going long-lived response to the 2005-10 rifting episode, with potential continued processes below the segment including a lower-crustal viscous response and magma movement. Continued long-term observations of surface deformation provide key constraints on tectono-magmatic processes in Afar.

1 Introduction

Magma plays a significant role in accommodating the final stages of continental break-up and the transition into early sea-floor spreading, and the Afar region of Ethiopia is uniquely placed to allow the observation of these processes sub-aerially (e.g. Ebinger, 2005; Kendall et al., 2005; Wright et al., 2012). Extensional strain in Afar is concentrated onto elongate rifting segments (Ebinger & Casey, 2001) which are maintained by rifting episodes that include effusive eruptions and dyking (Wright et al., 2006). Magmatic intrusions at these spreading segments produce time-dependent surface deformation, observable using time series of interferometric synthetic aperture radar (InSAR). These long time series can help separate surface deformation related to magma movement and viscoelastic relaxation, and have been used to constrain, and highlight the importance of viscous rheology in late-stage rifting (Pagli et al., 2014; J. Hamlyn et al., 2018).

1.1 Regional Setting

Upwelling of a mantle plume initiated rifting in Afar around 30 Ma with abundant flood-basalt volcanism, which has evolved into the ridge-ridge-ridge triple junction observed in Afar today (Wolfenden et al., 2004; Furman et al., 2006; Hammond et al., 2013). Relative to the Nubian Plate, the Arabian Plate is moving at a rate of 18-20 mm/yr to the NE (McClusky et al., 2010; ArRajehi et al., 2010), accommodated by the opening of the Red Sea Rift (RSR); while the Somalian Plate is moving to the SE at $\sim$ 6 mm/yr (Saria et al., 2014), accommodated by the Main Ethiopian Rift (MER) which is the northernmost segment of the larger East African Rift.

The crust beneath Afar is significantly thinned in comparison to the surrounding Ethiopian highlands and MER. Crustal thicknesses range from 20-45 km in the Ethiopian plateau, 18-30 km in central Afar, and 15-20 km in northern Afar (Tiberi et al., 2005; Bastow & Keir, 2011; Hammond et al., 2011; Lavayssière et al., 2018). Low seismic velocities indicate partial melt within the crust (Gallacher et al., 2016), particularly below volcanic segments in Afar (Stork et al., 2013; Hammond, 2014; Hammond & Kendall, 2016). Seismicity in the upper and lower crust along the Erta 'Ale volcanic segment (EAVS) also indicates the presence of melt below the Erta 'Ale and Alu-Dalafilla volcanic centres (Illsley-Kemp et al., 2018).

Active volcansim in Afar is largely concentrated within discrete rifting segments. The EAVS is the immediate on-land expression of the RSR. Erta 'Ale volcano on the EAVS is host to an lava lake with recent overflows in 2010 (Field et al., 2012; Barnie, Oppenheimer, & Pagli, 2016) and 2017, where a flank eruption indicated the presence of a shallow magma body at ~ 1 km depth (Moore et al., 2019). At Gada 'Ale, magma withdrawal and normal faulting caused subsidence from 1993-1996 (Amelung et al., 2000), and a dyke intrusion fed from a magma chamber 2-3 km below Dallol was detected in 2004 (Nobile et al., 2012). The 2008 eruption at Alu-Dalafilla was sourced from a ~ 1 km deep axis-aligned reservoir and a magma chamber at ~ 4 km depth (Pagli et al., 2012).

The largest recent volcano-tectonic rifting episode in Afar occurred from 2005-10 on the Dabbahu-Manda-Hararo volcanic segment (DMHVS) (Barnie, Keir, et al., 2016). The initial dyke in September 2005 ruptured the whole 60 km long segment, and intruded 2.4-2.6 km^3 of magma over ~ 2 weeks (Wright et al., 2006). Seismicity indicates that this dyke initiated beneath the Dabbahu and Gabho volcanoes at the northern end of

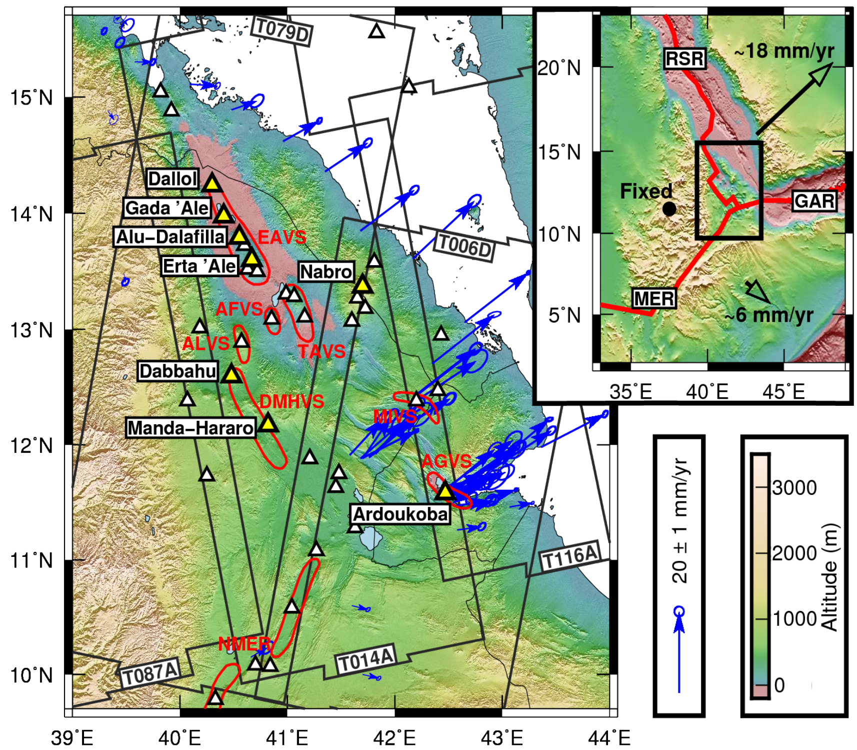

Figure 1. The Afar Rift with white triangles indicating Holocene volcanoes and key volcanoes highlighted in yellow. Simplified volcanic segments (VS) are shown in red: AFVS - Afdera, ALVS - Alayta, AGVS - Asal-Ghoubbet, DMHVS - Dabbahu-Manda-Hararo, EAVS - Erta 'Ale, MI - Manda-Inakir, NMER - Northern Main Ethiopian Rift, TAVS - Tat 'Ale. A subset of GNSS velocity vectors with 95% confidence error ellipses (blue arrows) from (King et al., 2019) show the long-term plate motions. Grey box outlines show the Sentinel-1 coverage from 3 ascending (T014A, T087A, T116A) and 2 descending (T006D, T079D) tracks. Inset map shows the relative movement of the Arabian and Somalian plates to the Nubian plate, with plate boundaries from Bird (2003). RSR - Red Sea Rift, GAR - Gulf of Aden Rift, MER - Main Ethiopian Rift.

the DMHVS, before focussing on the segment centre (Ayele et al., 2009). 13 subsequent dykes were emplaced between 2006-2010, drawing comparisons to the 1975-1984 Krafla rifting episode where extension in both settings is accommodated by magmatic intrusions (Hamling et al., 2010; Ferguson et al., 2010; Wright et al., 2012; Barnie, Keir, et al., 2016). Throughout the rifting episode there was an ongoing post-rifting response to the initial 2005 intrusion, which was modelled using magmatic sources in the upper crust, and the inflation of a deeper source at the segment centre, as viscoelastic relaxation alone was insufficient to reproduce geodetic observations (Grandin et al., 2010; Hamling et al., 2014).

The Manda-Inakir (MIVS) and Asal-Ghoubbet (AGVS) volcanic segments in southern Afar have also shown recent activity with the 1928-1929 eruption of Kammourta volcano in the MIVS (Audin et al., 1990), and the 1978 eruption at Ardoukoba volcano in the AGVS (Allard et al., 1979; Tarantola et al., 1979). Cattin et al. (2005) identified a post-rifting response in the AGVS to the 1978 eruption, with rift-perpendicular velocities decaying back to the long-term spreading rate 6-8 years after the eruption.

The Nabro Volcanic Range (NVR) is an off-axis volcanic-centre that sits within the Danakil Block, a rigid micro-plate which is moving away from Nubia with extension in Afar (Eagles et al., 2002). The NVR has hosted explosive eruptions at Dubbi volcano in 1861 (Wiart & Oppenheimer, 2000), and Nabro volcano in 2011 (J. E. Hamlyn et al., 2014; Goitom et al., 2015). Persistent subsidence was detected at Nabro for > 1 year following the 2011 eruption which was attributed to viscoelastic relaxation around a magma chamber at 6.4 ± 0.3 km depth (J. Hamlyn et al., 2018).

1.2 InSAR Velocity Methods & Applications in Afar

Methods for extracting a one-dimensional line-of-sight (LOS) displacement time series from a sequence or network of interferograms are well established. These small-baseline algorithms utilise multiple interferogram connections between acquisition dates to produce a more robust estimate of the incremental LOS ground displacement than a simple stacking of interferograms (Berardino et al., 2002; Lanari et al., 2007; Biggs et al., 2007). This methodology may be automated by software packages such as Π-RATE (Wang et al., 2012, and references therein), StaMPS (Hooper et al., 2012), GIAnT (Agram et al., 2013), and LiCSBAS (Morishita et al., 2020) in order to obtain linear displacement rates and uncertainties at each pixel, while reducing the effect of common sources of error such as atmospheric and orbital delays. These methods may be supplemented by additional filtering to remove the atmospheric phase screen (APS) from the time series, by firstly high-pass filtering in time, then low-pass filtering in space to calculate the APS, which is then removed from the time series (e.g. Sousa et al., 2011). The conventional method for APS calculation relies on the assumption that the atmospheric delay is not temporally correlated. With recent SAR missions providing shorter satellite revisit times, this assumption may no longer be appropriate. Previous studies have proposed improvements to the APS correction, including applying a global weather model (e.g. Jung et al., 2013), and accounting for the temporal variance of a pixel (e.g. Liu et al., 2011; Refice et al., 2011).

The only previous InSAR derived velocity map covering the whole Afar region was developed by Pagli et al. (2014), who used Π-RATE to produce a displacement time series between 2005-10. After removing large deformation steps associated with the DMH dyke intrusion events, Pagli et al. (2014) smoothed the time series by removing the APS, employing consistent Gaussian temporal and Butterworth spatial filters. Pagli et al. (2014) extracted 3D (east, north, vertical) velocities from ascending and descending LOS and Global Navigation Satellite Systems (GNSS) observations on a 10-20 km resolution mesh following the method of Wang and Wright (2012). Surface velocities between 2005-10 from Pagli et al. (2014) showed a long-term plate spreading rate of 15-20 mm/yr in Eastern Afar (relative to a stable Nubian plate), and large extension rates of ∼ 100 mm/yr at Dabbahu associated with the background response during the 2005-10 DMH rifting episode. Other InSAR velocity maps within Afar have focussed on individual rift segments, such as the DMHVS (Hamling et al., 2014) from 2006-10, the AGVS from 1997-2005 (Doubre & Peltzer, 2007), and around the Tendaho Graben from 2004-10 (Temtime et al., 2018).

In this study, we make use of the high temporal and spatial resolution data from the Sentinel-1 satellite to extract surface velocities from 2014-19 across the whole of the Afar region. We develop and apply a small baseline methodology with spatial and temporal variance weighted filtering to improve the removal of the APS, reference the data to a stable Nubia GNSS reference frame, and calculate 3D (vertical, rift-perpendicular horizontal, and rift-parallel horizontal) velocities.

2 Data Processing and Time Series Methods

2.1 Sentinel-1 Data

We use Sentinel-1A/B acquisitions from ascending tracks 14 (014A), 87 (087A), and 116 (116A), and descending tracks 6 (006D) and 79 (079D) between October 2014 and August 2019. For processing efficiency, we divide each track into 12 (∼ 250×250 km) frames (Table S1). We produce a network of geocoded unwrapped interferograms for each frame from single-look complex (SLC) images of each date using the LiCSAR software (González et al., 2016; Lazecky et al., in review.), which automates the mass production of interferograms using GAMMA (Werner et al., 2000). To reduce noise and data size, we multi-look the SLCs at 20:4 range to azimuth looks, equating to ∼ 100×100 m pixel size. We apply a topographic correction using an SRTM (Shuttle Radar Topography Mission) 3-arc-second (∼ 90 m resolution) DEM (Digital Elevation Model) (Farr & Kobrick, 2000), filter the interferograms using using a power spectrum filter (Goldstein et al., 1998), and unwrap using SNAPHU (Chen & Zebker, 2002). We manually quality check the interferogram network for each frame to remove interferograms with decorrelation, co-registration, or obvious unwrapping errors. We ensure that each epoch is connected to the network by a minimum of 3 interferograms by creating new interferograms as needed. Each interferogram is referenced to the mean value, excluding areas of deformation around volcanic centres.

To mitigate for atmospheric phase delay for each interferogram we compare the effectiveness of corrections from a linear trend of phase with elevation over the whole frame (e.g. Elliott et al., 2008), and the GACOS atmospheric model (e.g. Yu et al., 2017, 2018). For a linear phase-elevation trend correction, the mean root-mean-square (RMS) misfit for all 12 frames is reduced by 2.9 mm in comparison to the mean RMS misfit for all frames with no atmospheric correction. The GACOS correction gives a reduction in mean RMS misfit of 4.2 mm, but increases the RMS misfit in 29 % of interferograms. To reduce this we follow an approach similar to Shen et al. (2019), scaling the GACOS correction for each interferogram in order to minimise the resulting RMS misfit. This improves the atmospheric correction further, producing a reduction in mean RMS misfit of 5.7 mm (see Figure S1). In order to account for any residual topographic atmospheric signal in each frame, we remove a linear trend of phase with elevation from each epoch, after time series filtering.

2.2 Time Series

We apply an SBAS style methodology to invert for the displacement time series at each pixel in the frame, using all interferograms where a pixel is coherent. We assess the spatial and temporal variance of the time series by firstly, filtering using a Laplacian filter with a temporal width of 3 epochs and scale factor of 3, then calculating the RMS misfit from this trend at each pixel for every epoch. We calculate the spatial distribution of RMS misfit from the time series misfits at each point, and the temporal distribution of RMS misfit from the misfits of all pixels at each epoch (see Figure S2). To resolve the RMS misfit value of each pixel at every epoch, we scale the spatial RMS misfit map to the temporal RMS misfit value at each epoch (see Supplementary Materials). We use these error estimates to provide weights during time series filtering, and in the inversion of filtered displacement time series for average velocities.

In order to reduce the remaining APS in the displacement time series, we filter the time series using a high-pass temporal and a low-pass spatial filter to produce the APS, which we then remove from the time series. To calculate a low-pass temporal filter, we apply a weighted linear trend with a fixed temporal width of 1 year centred on each point. To calculate the weighting for the local trend, we use the RMS misfit as a proxy for standard error, and convert the RMS misfit values into weights using the Bi-Square function where no weight is given to RMS values that exceed 6 standard deviations of the local misfits (e.g. Cleveland & Devlin, 1988). We also scale these weights by their temporal distance from the target epoch of the local time series (see Supplementary Materials). Having calculated the low-pass temporal filter, we remove it from the time series to create a high-pass temporal filter. We then apply a Gaussian spatial filter with a half-width of $\sim$ 2 km in order to resolve the APS for each epoch.

After we remove the APS, we remove a planar ramp in space and a linear trend with height to correct for any remnant long-wavelength and elevation-correlated atmospheric delay. We later correct for long-wavelength deformation using GNSS observations. For each frame, we compute the average velocity at each pixel by inverting for a single linear trend through time, allowing for a constant offset. We produce a variance-covariance matrix (VCM) for each pixel, treating the temporal variation of the scaled RMS misfit as independent errors. By including the VCM in the inversion, we can quantify the uncertainty of the resulting velocities.

De Zan et al. (2015) demonstrate how a potential systematic phase-bias in interferograms with decreasing temporal baseline can influence the resulting time series. We test the magnitude of this bias by selecting consecutive 12, 24, and 36-day interferograms from frame 079D_07694_131313 covering $\sim$ 1 year (see Figure S3). We use a 'daisy-chain' stack approach to resolve the cumulative displacements from the 12, 24, and 36 day unwrapped interferograms between December 2017 and February 2019. Any differences between these stacks indicates the presence of phase-bias and/or unwrapping errors. We find residual differences between the 12 and 24-day, and 12 and 36-day stacks of up to 50 mm, and residuals of up to 10 mm between the 24 and 36-day stacks. While this indicates that the 12-day interferograms are susceptible to a phase-bias, we find that removing the 12-day interferograms from the network effects our displacement time series by $<$ 5 mm per epoch, and our average velocities by $<$ 1 mm/yr. While we are not able to account for any bias in the 36-day interferograms, Ansari et al. (2020) indicate that the velocity bias is small in comparison to 12-day interferograms.

2.3 3D Velocities

We tie frames together within their respective tracks by sub-sampling the InSAR data points to a 5×5 km spacing in the overlap between frames, and 10×10 km spacing elsewhere, then solving for and removing a planar ramp for each frame that minimises residuals in the along-track frame overlap regions. Removing these ramps does not bias the results as long-wavelength signals are later corrected using GNSS. In the frame overlap region, we use the mean value of LOS velocity for each point. We find that using linear ramps to combine frames within tracks produces the fewest boundary artefacts when compared to using a single offset value calculated from the median value in the frame overlap region, or solving for a 2D quadratic function for each frame. Boundary artefacts within tracks can occur due to differences between frames in time series length, the variation in acquisition dates used, relative weighting during time-series filtering, and orbital ramp removal. Although in principle it would be possible to only process and use interferograms that cover the whole along-track extent of the study region, this would require excluding several epochs where data were not acquired over the whole area, resulting in truncated time series.

To reference the LOS velocity in each track to a stable Nubian plate, we use a network of 105 GNSS stations in the Afar region to characterise long-wavelength plate motions. The data are a subset of the GeoPRISMS community velocity field for East Africa in a Nubia-fixed International Terrestrial Reference Frame (ITRF2014) (King et al., 2019). We remove 32 stations in central Afar where the velocities are dominated by the ground motions associated with the 2005-10 DMH rifting episode. As the resulting network is sparse, with the majority of stations concentrated in Eastern Afar and few points on the Nubian and Somalian plates; we add 17 additional fabricated GNSS stations on the stable Nubian plate, with an assumed zero velocity (with uncertainties of ± 1 mm/yr and ± 2 mm/yr in the horizontal and vertical components), to help constrain the velocity field where data are sparse. We project East and North GNSS horizontal velocities into the rift-perpendicular (e.g. Hamling et al., 2014), and rift-parallel directions, oriented at 61°N and -29°N respectively.

From this network, we interpolate a smooth GNSS velocity field in the rift-perpendicular and rift-parallel directions over the whole Afar region at 100×100 m grid spacing (Figure S4) using the natural neighbour algorithm (e.g. Boissonnat & Cazals, 2002). As the additional pseudo-observations define where this interpolated field reaches zero velocity, we selected these points such that they are on the Nubian plate, away from the rift border faults. We are not concerned with the precise locations, as where the interpolated velocity field reaches zero does not significantly influence the data within the Afar from the Rift. We estimate the error in the interpolated velocities by systematically removing each GNSS station from the network, interpolating new velocity fields in the rift-perpendicular and rift-parallel directions from the reduced network, then calculating the residual between the interpolated fields and the GNSS observation. We take the standard deviation of these residuals as the error in the rift-perpendicular and rift-parallel GNSS velocity field.

We sub-sample the InSAR LOS track velocities as previously, then extract points where there are ascending, descending, and interpolated GNSS data. We also mask points around the active rift segments so that volcanic ground deformation does not interfere with the referencing to the long-term plate motions. Using these points, we solve for the 3D velocity (rift-perpendicular, rift-parallel, vertical) at each point and a residual 2D (East, North) quadratic function for each track. We remove the respective quadratic from each InSAR track to resolve LOS velocity in a stable Nubia reference frame. The resulting LOS velocities and standard deviations are shown in Figures 2 and S5 respectively.

In order to resolve a full 3D velocity field (vertical, rift-perpendicular horizontal, rift-parallel horizontal) at 100×100 m resolution, we use the smooth rift-parallel GNSS field to provide a constraint on the rift-parallel velocity at each point, as the rift-parallel velocities are small in comparison to the rift-perpendicular and vertical velocities. We include this constraint with the ascending and descending LOS InSAR observations to calculate 3D velocities at each point using a least-squares inversion (Wright et al., 2004; Hussain et al., 2016; Weiss et al., 2020). The decomposition of InSAR LOS velocities (L) into rift-perpendicular ($H1$), rift-parallel ($H2$), and vertical (Z) velocities is shown in Equation 1 for the incidence angle (θ), satellite heading (α), rift angle from North (ϕ). We weight the inversion and resolve uncertainties by including a diagonal VCM using the previously calculated variance at each point.

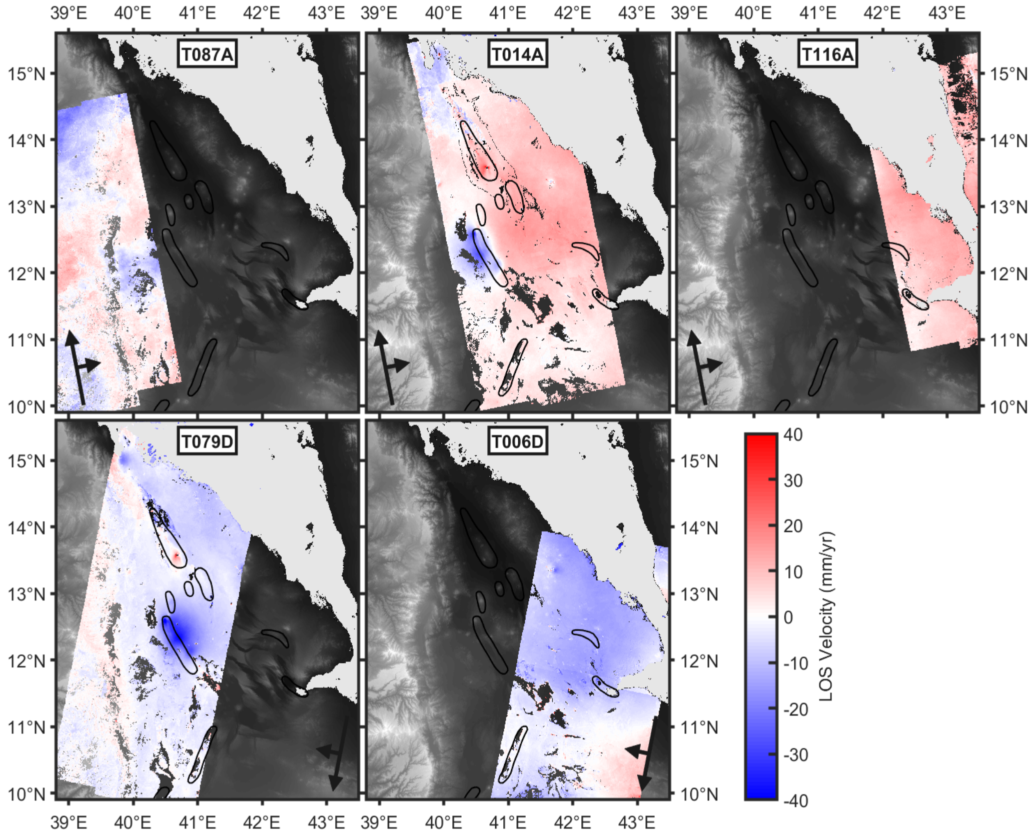

Figure 2. LOS average velocities over the Afar region between November 2014 and August 2019 from Sentinel-1 tracks T087A, T014A, T116A, T079D, and T006D. LOS velocities are referenced to a stable Nubia reference frame using long-term plate motions from the regional GNSS network (King et al., 2019). Arrows indicate the track look directions, and the volcanic segments are shown as black outlines.

Results (Figure 3), discussed in Section 3, show both the long-term plate motion and surface deformation associated with magmatism. As we use the interpolated GNSS velocity field as an additional constraint in the rift-parallel direction, the resulting rift-parallel error estimates are lower than the rift-perpendicular errors, which we calculate using only the InSAR observations to retain high spatial resolution (see Figure 3).

$$L = \begin{bmatrix} -sin(\theta)cos(\alpha+\phi) + sin(\theta)sin(\alpha+\phi) - cos(\theta) \end{bmatrix} \begin{bmatrix} H1 \\ H2 \\ Z \end{bmatrix} \tag{1}$$

3 Key Findings & Discussion

3.1 Plate Motions & Rift Focussing

Our 2014-2019 horizontal velocity maps (Figure 3) show the rift-perpendicular extension over the Afar rift at rates of up to 25 ± 5 mm/yr, with negligible motions in the rift-parallel direction. We also observe the 'trapdoor' motion of the Danakil micro-plate relative to the stable Nubian plate (Kidane, 2016), where rift-perpendicular extension in the RSR is gradually transferred into Afar between 13-16°N. Areas of noise up to ± 10 mm/yr over the Ethiopian highlands region on the Nubain plate, are highlighted in the standard deviation maps shown in Figure 3. The regions of high error in T087A, and the northern-most portion of T014A (see Figure S5), are a result of the shorter time series length in these regions producing more uncertainty in the long-term velocity estimates. Elsewhere, errors of up to $\pm$ 5 mm/yr are likely due to uncorrected atmospheric delays, and artefacts over track boundaries, where we are unable to account for small LOS velocity variations between overlapping tracks.

Profiles taken across the rift highlight the focussing of extension in Afar. Profiles covering the Alid graben, at northern-most tip of the Afar rift (Figures 4B and 5B), show that a broad uplift and extensional signal of up to $\sim$ 20 mm/yr is centred within $\pm$ 10-15 km of the rift axis. This may be indicative of deep magmatic intrusion in an area with the smallest background extension rates throughout Afar, but comparable to extension rates at the active volcanic islands at the southern end of the oceanic RSR (Eyles et al., 2018). Profiles traversing the EAVS in the Danakil Depression (Figures 4C and 5C) highlight that the majority of extension here is focussed into a region within $\pm$ 15-20 km of the rift axis. We also observe subsidence on the EAVS between the Erta 'Ale and Alu

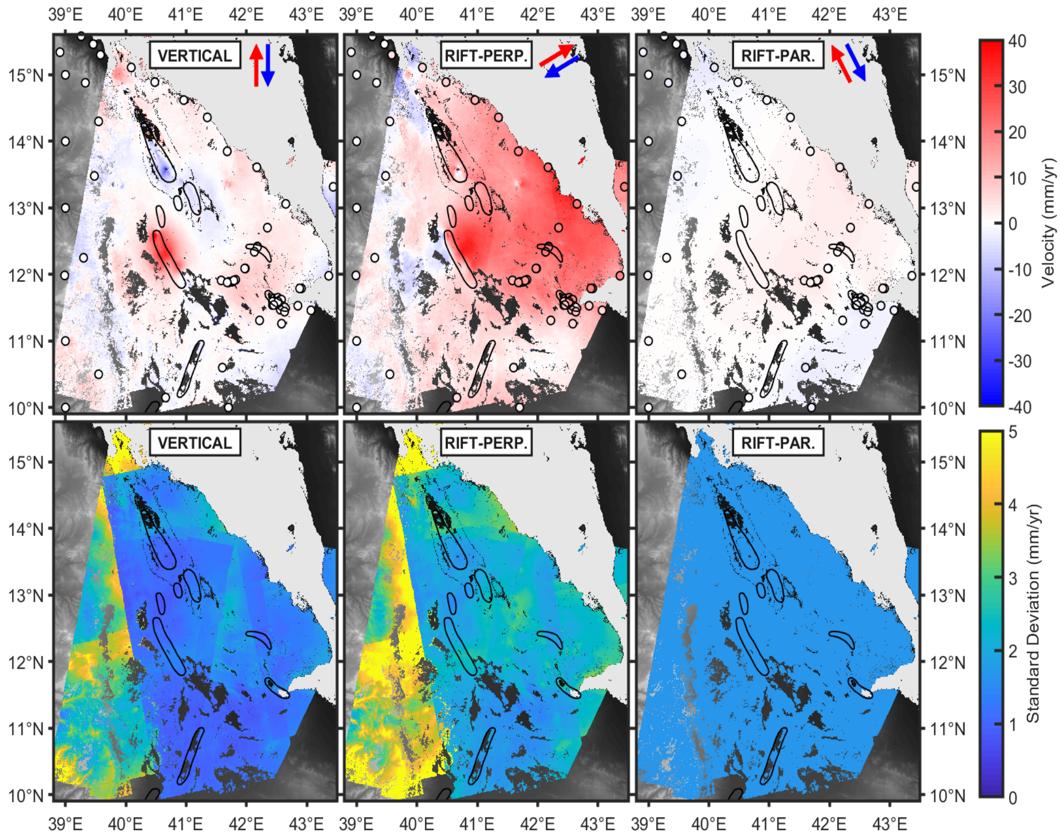

Figure 3. Vertical, rift-perpendicular, and rift-parallel average velocities and standard deviation over the Afar region between November 2014 and August 2019. All velocities are referenced to a stable Nubian plate. Vertical velocities are positive upwards, rift-perpendicular velocities are positive to the NE (61°N), and rift-parallel velocities are positive to the NW (-29°N). Standard deviation colour-scale is limited to 5 mm/yr to highlight variation in regions of low variance. Maximum standard deviations are (2 s.f.): 7.2 mm/yr (vertical), 9.5 mm/yr (rift-perpendicular), and 1.7 mm/yr (rift-parallel). GNSS stations are shown as circles with GNSS velocities on the same colour-scale as the InSAR velocities, and volcanic segments as black outlines.

Dalafilla volcanoes (Figure 4C), which could be linked to magma withdrawal associated with the 2017-19 eruption at Erta 'Ale (Moore et al., 2019). Profiles between the EAVS and the DMHVS (Figure 5C) show that extension in this region is shared between the ALVS and the TAVS, and focussed to within ± 10-20 km of the rift segments.

Profiles covering the DMHVS (Figures 4D and 5D) also show that the long-term extension is concentrated near the rift-axis, with only small variations in rift-perpendicular velocity away from ± 20-30 km of the segment centre. Elevated velocities close to the segment centre are associated with the 2005-10 DMHVS rifting episode, and are discussed

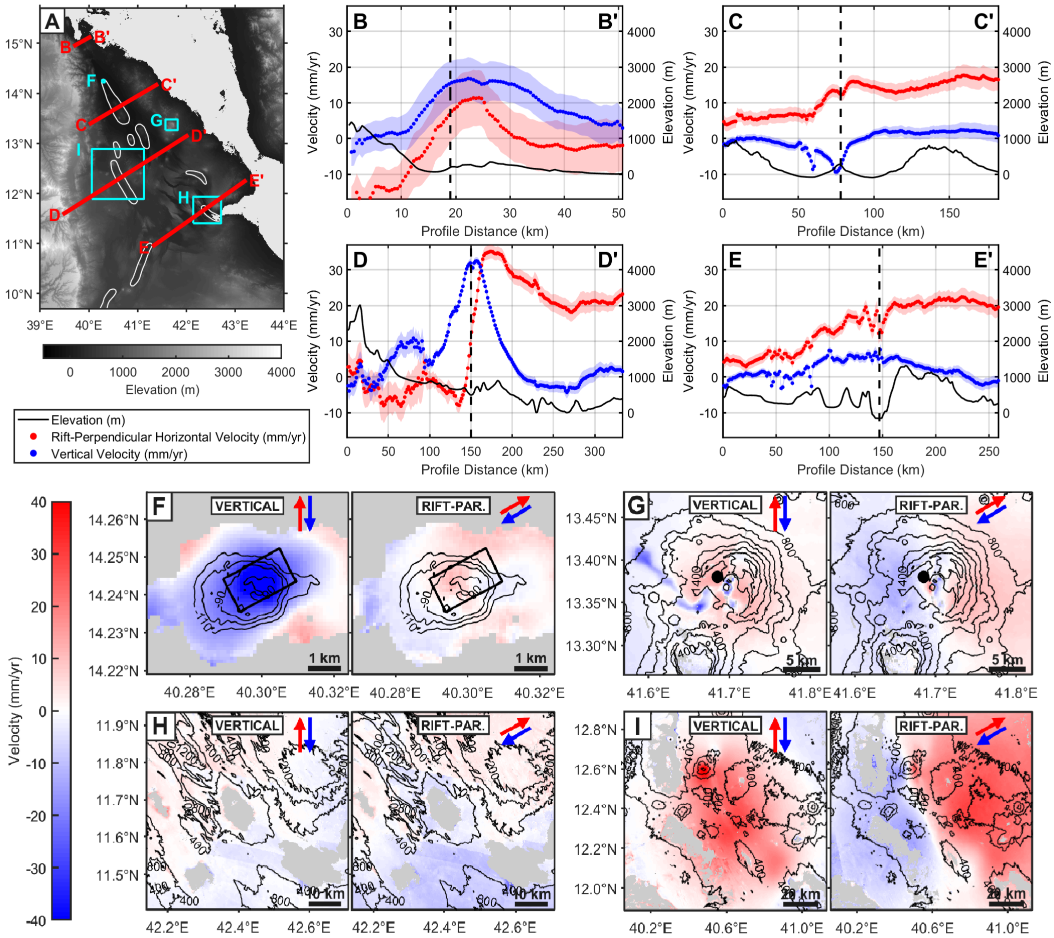

Figure 4. (B-E) Vertical (blue, positive up) and rift-perpendicular (red, positive towards 61°N) velocities over 4 10 km wide cross-rift profiles marked on insert map, covering (B) the northern tip of the Afar triangle, (C) the Erta 'Ale volcanic segment, (D) the Dabbahu-Manda-Hararo volcanic segment (DMHVS), and (E) the Asal-Ghoubbet volcanic segment (AGVS). Black lines show surface elevation along the profiles, with vertical dashed lines indicating the location of the major rift axis on the profile. (F-I) Vertical and rift-perpendicular velocity maps at (F) Dallol volcano, (G) Nabro volcano, (H) the AGVS, and (I) the DMHVS. Velocities in each subset are referenced to the local background mean value, with contours indicating elevation. The location of modelled deformation sources for a 0.9-1.3 km deep sill (Okada, 1985) at Dallol (F, Figure S6) and a 5.5-6.8 km deep point source (Mogi, 1958) at Nabro (G, Figure S7) are shown as black outlines.

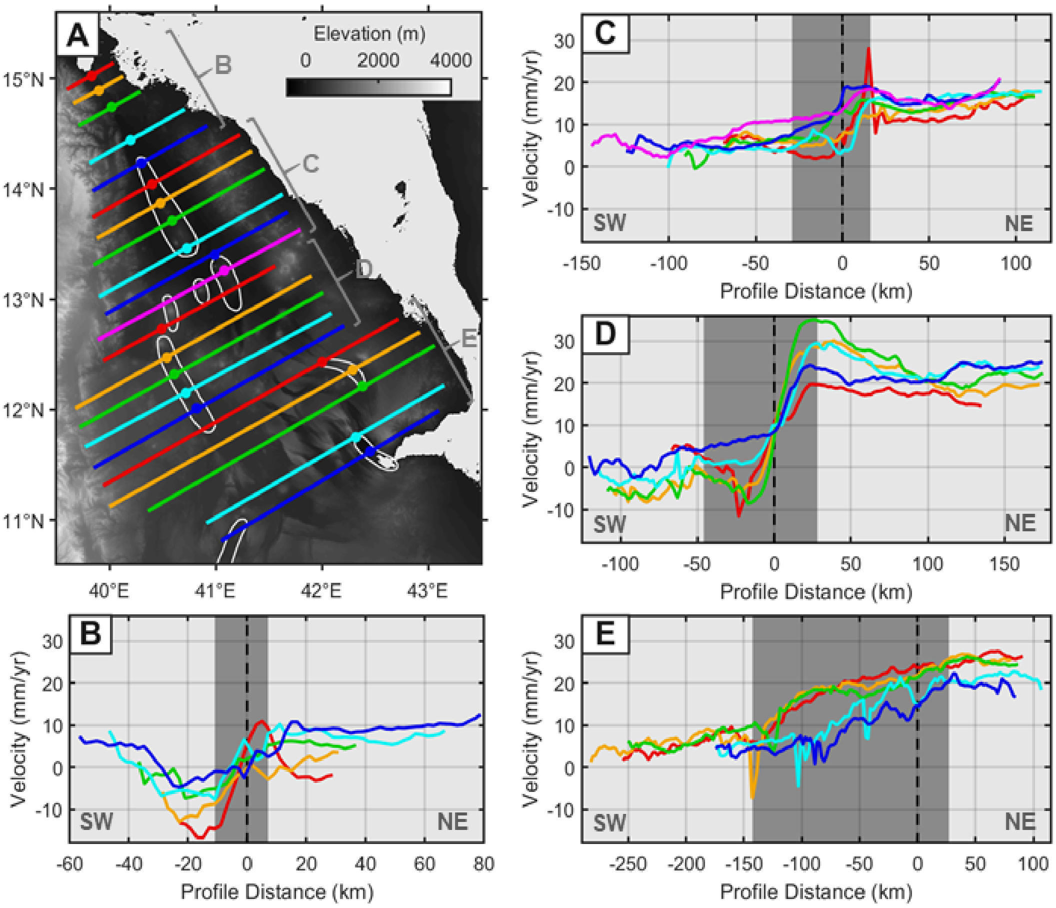

Figure 5. Map of 21 10 km wide rift-perpendicular velocity (relative to stable Nubia, positive towards 61°N) profiles over the Afar rift (A), with rift segments outlined in white. To help distinguish between profiles, profiles alternate between solid and dashed lines. The velocity profiles cover northern Afar (B), the Erta 'Ale and Tat 'Ale segments (C), the Dabbahu-Manda-Hararo segment (D), and southern Afar (E). The standard deviation of rift-perpendicular velocities varies from ± 2-7 mm/yr (see Figure 3). Profile distances are relative to the rift axis, with positive towards the NE. The location of the rift axis is marked by circles on the map (A), and dashed black lines on profiles (B-E). Grey shading on the profiles indicates the region where the majority of rift extension is accommodated.

in Section 3.2. Profiles over southern Afar and the AGVS (Figures 4E and 5E) show a more distributed pattern of extension with an increase in rift-perpendicular velocities 80-160 km to the SW of the rift axis, before velocities stabilise at $\sim$ 20 mm/yr on the Danakil micro-plate within 10-20 km to the NE of the rift axis. In southern Afar, extension between 2014-19 may be largely accommodated by tectonic rather than magmatic mechanisms, with strain being distributed across a sequence of horst and graben structures.

Our results indicate that at the more mature segments with active magmatism in central and northern Afar, extension is largely focussed to within ± 15-30 km of the rift axis; while at less mature segments without active magmatism in southern Afar, extension may be distributed of a over 90-180 km. The broad distribution of strain in southern Afar is in general agreement with 1992-2010 GNSS observations from Kogan et al.

(2012), who suggest that extension along a profile in southern Afar occurs over ~ 175 km. Kogan et al. (2012) also suggest that extension becomes more distributed with rift development. In contrast, our results suggest an increase in focussing with rift maturity during late-stage continental break-up, in keeping with strain localisation assisting the transition into oceanic spreading centres.

3.2 Magmatic Deformation

Figure 4 highlights the localised surface deformation at Dallol (4F) and Nabro (4G) volcanoes, and at the DMHVS (4I), where localised deformation, likely associated with magma migration, is visible. Figure 4H over the AGVS indicates the lack of magma related deformation at this segment between 2014-19. As magmatic deformation may not be steady in time, we look at time series for points located in the middle of these centres. Time series of vertical displacements at the Dallol, Nabro, Dabbahu, and Manda-Hararo volcanic centres show that the deformation is linear through time, indicating that the velocities are representative (Figure 6). For Erta 'Ale volcano, we select a point ~ 2 km to the north of the summit caldera in order to avoid the step surface deformation associated with a dyke intrusion in January 2017 (Moore et al., 2019). Following this intrusion the Erta 'Ale edifice shows linear subsidence at a rate of 15 ± 4 mm/yr (Figure 6).

At Dallol volcano, at the northern end on the EAVS, we observe a high rate of subsidence of up to 45 ± 4 mm/yr, with negligible horizontal movement. The subsidence signal is focussed on the central cone at Dallol. We model this signal using the Markov-Chain Monte-Carlo Geodetic Bayesian Inversion Software (GBIS) (Bagnardi & Hooper, 2018). For the T014A and T079D LOS deformation between 2014-19, we test source ge-

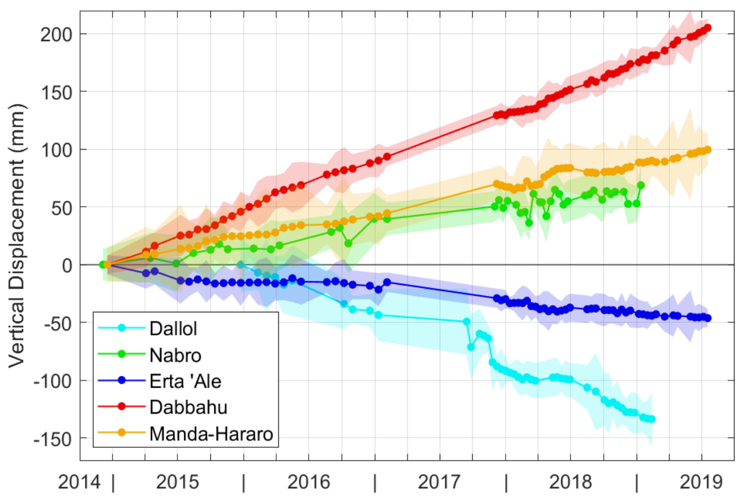

Figure 6. 2014-19 time series of vertical displacements (uplift positive) with 1 standard deviation estimates, at 5 deforming volcanic centres in Afar. The points used for the time series are representative of the whole edifice deformation and are positioned at the centre of the volcanic edifice; with the exception of Erta 'Ale where the point selected is ~ 2 km North of the summit lava lake in order to avoid surface deformation associated with the Jan 2017 dyke intrusion event (Moore et al., 2019). Coordinates of points used for each volcanic centre: Dallol - 40.3°E/14.243°N, Nabro - 41.685°E/13.38°N, Erta 'Ale - 40.65°E/13.62°N, Dabbahu - 40.48°E/12.58°N, Manda-Hararo - 40.88°E/12.13°N.

ometries including a point pressure source (Mogi, 1958), a planar dislocation (Okada, 1985), and a penny-shaped crack (Fialko et al., 2001). We find that a $\sim 1\times2$ km horizontal sill at 0.9-1.3 km depth with ~ 0.27 m of contraction gives the lowest residual RMS misfit (Figure S6). This is in agreement with Nobile et al. (2012) who inferred the presence of a deflating magma body at 1.5-3.3 km depth beneath Dallol between 2004-06.

At Nabro volcano, we observe edifice uplift and extension at rates of up to 12 ± 3 mm/yr, combined with the subsidence of lava flows from the 2011 eruption (J. E. Hamlyn et al., 2014), and a highly localised subsidence and contraction signal of up to 14 ± 3 mm/yr at the centre of the Nabro caldera. This uplift of the Nabro edifice shows a change from InSAR observed subsidence of 150-200 mm/yr from 2011-12, after the 2011 eruption (J. Hamlyn et al., 2018). As our vertical displacement time series (Figure 6) indicates that the uplift at Nabro is linear between 2014-19, we suggest that this post-eruption edifice subsidence must have stopped between 2012-14. We model T006D, T014A, and T079D LOS observations at Nabro volcano between 2014-19 using a point pressure source (Mogi, 1958), and penny-shaped crack (Fialko et al., 2001) using GBIS (Bagnardi & Hooper, 2018). Figure S7 shows the optimal Mogi source at 5.5-6.8 km depth with a volume increase of $7\text{-}11\times10^6$ m^3. The location of this source is in agreement with the magma chamber at 6.4 ± 0.3 km depth inferred by (J. Hamlyn et al., 2018) between 2011-12, indicating re-charge of the melt storage below Nabro volcano.

After the initial 2005 intrusion at the DMHVS, background uplift and rift-perpendicular extension continued throughout the 2005-10 rifting episode at rates of up to 80-240 mm/yr and 110-180 mm/yr respectively, from 2006-10 at the segment centre (Pagli et al., 2014; Hamling et al., 2014). We show that this uplift and extension is ongoing between 2014-19 at average rates of 33 ± 4 mm/yr and 37 ± 4 mm/yr respectively (Figure 4c,h). Our vertical velocities also show that an area of ~ 20 mm/yr subsidence from 2006-10 at the southern end of the DMHVS (40.9°E/12.1°N) uplifts at an average rate of 18 ± 4 mm/yr from 2014-19. This decaying post-rifting response to the initial 2005 intrusion may be indicative of continued magma movement beneath the DMHVS and/or a time-dependant viscous response due to a more ductile rheology generated from repeated intrusions at the rift segment.

4 Conclusions

We develop Sentinel-1 displacement time series at 100×100 m resolution between 2014-19 over 3 ascending and 2 descending tracks, covering the whole Afar rift. We implement a RMS misfit weighted APS correction to clean the time series, and produce average velocity maps for each frame. Using GNSS observations of long-term plate motions, we reference the InSAR velocities to the stable Nubian plate, and convert LOS to 3D velocities (vertical, rift-perpendicular, rift-parallel).

We are able to resolve deformation at individual volcanic centres, with subsidence of 45 ± 4 mm/yr at Dallol volcano, consistent with the deflation of a shallow sill at 0.9-1.3 km depth. We also show that edifice uplift at Nabro volcano of 12 ± 3 mm/yr is sourced from a magma chamber at 5.5-6.8 km depth, consistent with the source of post-eruption subsidence observed between 2011-12 (J. Hamlyn et al., 2018).

Pagli et al. (2014) and Hamling et al. (2014) identify vertical and rift-perpendicular horizontal surface velocities between 2006-10 of 80-240 mm/yr and 110-180 mm/yr, respectively associated with a background post-rift response to the initial 2005 dyking episode at the DMHVS. We show that this response is ongoing between 2014-19, but at lower rates of 33 ± 4 mm/yr and 37 ± 4 mm/yr respectively. We suggest that this ~ 15 year response to the 2005 dyke intrusion is indicative of continued magma movement and/or time-dependant viscous processes within the crust below the rift segment.

We resolve the long-term motion of the Danakil micro-plate with rift-perpendicular velocities of up to 25 ± 5 mm/yr, with negligible motions in the rift-parallel direction. From cross-rift profiles, we find that extension is largely focussed to within ± 15-30 km of the rift-axis on the active magmatic segments in northern Afar, while strain in southern Afar is distributed across 90-180 km of the rift. This trend of increased focussing of extension with rift maturity is in contrast to the trend suggested by Kogan et al. (2012), but consistent with strain localisation assisting the transition into oceanic spreading centres.

Acknowledgments

All Sentinel-1 data is sourced from the European Union Copernicus Programme. We perform data processing on the JASMIN facility, operated by the Centre for Environmental Data Analysis (CEDA), and post-processing and figure generation using MATLAB and GMT. Processed LiCSAR interferograms are available in the Centre for Environmental Data Analysis (CEDA) archive (`http://archive.ceda.ac.uk`) here: `http://data.ceda.ac.uk/neodc/comet/data/licsar_products`. This work was funded by the NERC RiftVolc project (NE/L013649/1), and supported by the Centre for Observation and Modelling of Earthquakes, Volcanoes, and Tectonics (COMET).

References

Agram, P., Jolivet, R., Riel, B., Lin, Y., Simons, M., Hetland, E., … Lasserre, C. (2013). New radar interferometric time series analysis toolbox released. *Eos, Transactions American Geophysical Union*, *94*(7), 69–70.

Allard, P., Tazieff, H., & Dajlevic, D. (1979). Observations of seafloor spreading in Afar during the November 1978 fissure eruption. *Nature*, *279*(5708), 30–33. doi: 10.1038/279030a0

Amelung, F., Oppenheimer, C., Segall, P., & Zebker, H. (2000). Ground deformation near Gada 'Ale volcano, Afar, observed by radar interferometry. *Geophysical Research Letters*, *27*(19), 3093–3096. doi: 10.1029/2000GL008497

Ansari, H., De Zan, F., & Parizzi, A. (2020). Study of Systematic Bias in Measuring Surface Deformation with SAR Interferometry. *IEEE Transactions on Geoscience and Remote Sensing*, 1-1.

ArRajehi, A., McClusky, S., Reilinger, R., Daoud, M., Alchalbi, A., Ergintav, S., … Kogan, L. (2010). Geodetic constraints on present-day motion of the Arabian Plate: Implications for Red Sea and Gulf of Aden rifting. *Tectonics*, *29*(TC3011). doi: 10.1029/2009TC002482

Audin, J., Vellutini, P. J., Coulon, C., Piguet, P., & Vincent, J. (1990). The 1928-1929 eruption of Kammourta volcano - Evidence of tectono-magmatic activity in the Manda-Inakir rift and comparison with the Asal Rift, Afar depression, Republic of Djibuti. *Bulletin of Volcanology*, *52*, 551–561.

Ayele, A., Keir, D., Ebinger, C., Wright, T. J., Stuart, G. W., Buck, W. R., … Sholan, J. (2009). September 2005 mega-dike emplacement in the Manda-Harraro nascent oceanic rift (Afar depression). *Geophysical Research Letters*, *36*(L20306). doi: 10.1029/2009GL039605

Bagnardi, M., & Hooper, A. (2018). Inversion of Surface Deformation Data for Rapid Estimates of Source Parameters and Uncertainties: A Bayesian Approach. *Geochemistry, Geophysics, Geosystems*, *19*. doi: 10.1029/2018GC007585

Barnie, T. D., Keir, D., Hamling, I., Hofmann, B., Belachew, M., Carn, S., … Wright, T. (2016). A multidisciplinary study of the final episode of the Manda Hararo dyke sequence, Ethiopia, and implications for trends in volcanism during the rifting cycle. *Geological Society, London, Special Publications*, *420*, 149–163. doi: 10.1144/SP420.6

Barnie, T. D., Oppenheimer, C., & Pagli, C. (2016). Does the lava lake of Erta Ale volcano respond to regional magmatic and tectonic events? An investigation using Earth Observation data. *Geological Society, London, Special Publications*, *420*, 181–208. doi: 10.1144/SP420.15

Bastow, I. D., & Keir, D. (2011). The protracted development of the continent-ocean transition in Afar. *Nature Geoscience*, *4*(4), 248–250. doi: 10.1038/ngeo1095

Berardino, P., Fornaro, G., Lanari, R., & Sansosti, E. (2002). A new algorithm for surface deformation monitoring based on small baseline differential SAR interferograms. *IEEE Transactions on Geoscience and Remote Sensing*, *40*(11), 2375–2383. doi: 10.1109/TGRS.2002.803792

Biggs, J., Wright, T., Lu, Z., & Parsons, B. (2007). Multi-interferogram method for measuring interseismic deformation: Denali Fault, Alaska. *Geophysical Journal International*, *170*(3), 1165–1179. doi: 10.1111/j.1365-246X.2007.03415.x

Bird, P. (2003). An updated digital model of plate boundaries. *Geochemistry, Geophysics, Geosystems*, *4*(3). doi: 10.1029/2001GC000252

Boissonnat, J.-D., & Cazals, F. (2002). Smooth surface reconstruction via natural neighbour interpolation of distance functions. *Computational Geometry*, *22*(1-3), 185–203.

Cattin, R., Doubre, C., de Chabalier, J. B., King, G., Vigny, C., Avouac, J. P., & Ruegg, J. C. (2005). Numerical modelling of quaternary deformation and post-rifting displacement in the Asal-Ghoubbet rift (Djibouti, Africa). *Earth and Planetary Science Letters*, *239*(3-4), 352–367. doi: 10.1016/j.epsl.2005.07.028

Chen, C. W., & Zebker, H. A. (2002). Phase unwrapping for large SAR interferograms: Statistical segmentation and generalized network models. *IEEE Transactions on Geoscience and Remote Sensing*, *40*(8), 1709–1719.

Cleveland, W. S., & Devlin, S. J. (1988). Locally weighted regression: an approach to regression analysis by local fitting. *Journal of the American statistical association*, *83*(403), 596–610.

De Zan, F., Zonno, M., & Lopez-Dekker, P. (2015). Phase inconsistencies and multiple scattering in SAR interferometry. *IEEE Transactions on Geoscience and Remote Sensing*, *53*(12), 6608–6616.

Doubre, C., & Peltzer, G. (2007). Fluid-controlled faulting process in the Asal Rift, Djibouti, from 8 yr of radar interferometry observations. *Geology*, *35*(1), 69–72. doi: 10.1130/G23022A.1

Eagles, G., Gloaguen, R., & Ebinger, C. (2002). Kinematics of the Danakil microplate. *Earth and Planetary Science Letters*, *203*(2), 607–620. doi: 10.1016/S0012-821X(02)00916-0

Ebinger, C. J. (2005). Continental break-up: the East African perspective. *Astronomy & Geophysics*, *46*(2), 2–16.

Ebinger, C. J., & Casey, M. (2001). Continental breakup in magmatic provinces: An Ethiopian example. *Geology*, *29*(6), 527–530. doi: 10.1130/0091-7613(2001)029⟨0527:CBIMPA⟩2.0.CO;2

Elliott, J. R., Biggs, J., Parsons, B., & Wright, T. J. (2008). InSAR slip rate determination on the Altyn Tagh Fault, northern Tibet, in the presence of topographically correlated atmospheric delays. *Geophysical Research Letters*, *35*(12), 1–5. doi: 10.1029/2008GL033659

Eyles, J. H., Illsley-Kemp, F., Keir, D., Ruch, J., & Jónsson, S. (2018). Seismicity associated with the formation of a new island in the Southern Red Sea. *Frontiers in Earth Science*, *6*, 141.

Farr, T. G., & Kobrick, M. (2000). Shuttle Radar Topography Mission produces a wealth of data, Eos Trans. *Eos, Transactions American Geophysical Union*, *81*(48), 583–585. doi: 10.1029/EO081i048p00583

Ferguson, D. J., Barnie, T. D., Pyle, D. M., Oppenheimer, C., Yirgu, G., Lewi, E., … Hamling, I. (2010). Recent rift-related volcanism in Afar, Ethiopia.

Earth and Planetary Science Letters, *292*(3-4), 409–418. doi: 10.1016/j.epsl.2010.02.010

Fialko, Y., Khazan, Y., & Simons, M. (2001). Deformation due to a pressurized horizontal circular crack in an elastic half-space, with applications to volcano geodesy. *Geophysical Journal International*, *146*(1), 181–190.

Field, L., Barnie, T., Blundy, J., Brooker, R. A., Keir, D., Lewi, E., & Saunders, K. (2012). Integrated field, satellite and petrological observations of the November 2010 eruption of Erta Ale. *Bulletin of Volcanology*, *74*, 2251–2271. doi: 10.1007/s00445-012-0660-7

Furman, T., Bryce, J., Rooney, T., Hanan, B., Yirgu, G., & Ayalew, D. (2006). Heads and tails: 30 million years of the Afar plume. *Geological Society, London, Special Publications*, *259*, 95–119. doi: 10.1144/GSL.SP.2006.259.01.09

Gallacher, R. J., Keir, D., Harmon, N., Stuart, G., Leroy, S., Hammond, J. O., … Ahmed, A. (2016). The initiation of segmented buoyancy-driven melting during continental breakup. *Nature Communications*, *7*(13110). doi: 10.1038/ncomms13110

Goitom, B., Oppenheimer, C., Hammond, J. O., Grandin, R., Barnie, T., Donovan, A., … Berhe, S. (2015). First recorded eruption of Nabro volcano, Eritrea, 2011. *Bulletin of Volcanology*, *77*(85), 1–21. doi: 10.1007/s00445-015-0966-3

Goldstein, J., Reed, I., & Scharf, L. (1998). A multistage representation of the Wiener filter based on orthogonal projections. *IEEE Transactions on Information Theory*, *44*(7), 2943–2959. doi: 10.1109/18.737524

González, P. J., Walters, R. J., Hatton, E. L., Spaans, K., & Hooper, A. (2016). LiCSAR: Tools for automated generation of Sentinel-1 frame interferograms. *AGU Fall Meeting*.

Grandin, R., Socquet, A., Doin, M. P., Jacques, E., De Chabalier, J. B., & King, G. C. (2010). Transient rift opening in response to multiple dike injections in the Manda Hararo rift (Afar, Ethiopia) imaged by time-dependent elastic inversion of interferometric synthetic aperture radar data. *Journal of Geophysical Research: Solid Earth*, *115*(B09403). doi: 10.1029/2009JB006883

Hamling, I. J., Wright, T. J., Calais, E., Bennati, L., & Lewi, E. (2010). Stress transfer between thirteen successive dyke intrusions in Ethiopia. *Nature Geoscience*, *3*(10), 713–717. doi: 10.1038/ngeo967

Hamling, I. J., Wright, T. J., Calais, E., Lewi, E., & Fukahata, Y. (2014). InSAR observations of post-rifting deformation around the Dabbahu rift segment, Afar, Ethiopia. *Geophysical Journal International*, *197*, 33–49. doi: 10.1093/gji/ggu003

Hamlyn, J., Wright, T., Walters, R., Pagli, C., Sansosti, E., Casu, F., … others (2018). What causes subsidence following the 2011 eruption at Nabro (Eritrea)? *Progress in Earth and Planetary Science*, *5*(1), 31.

Hamlyn, J. E., Keir, D., Wright, T. J., Neuberg, J. W., Goitom, B., Hammond, J. O. S., … Grandin, R. (2014). Seismicity and subsidence following the 2011 Nabro eruption, Eritrea: Insights into the plumbing system of an off-rift volcano. *Journal of Geophysical Research: Solid Earth*, *119*, 8267–8282. doi: 10.1002/2014JB011395

Hammond, J. O. S. (2014). Constraining melt geometries beneath the Afar Depression, Ethiopia from teleseismic receiver functions: The anisotropic H-κ stacking technique. *Geochemistry, Geophysics, Geosystems*, *15*(4), 1316–1332.

Hammond, J. O. S., & Kendall, J. M. (2016). Constraints on melt distribution from seismology: a case study in Ethiopia. *Geological Society, London, Special Publications*, *420*, 127–147. doi: 10.1144/SP420.14

Hammond, J. O. S., Kendall, J. M., Stuart, G. W., Ebinger, C. J., Bastow, I. D., Keir, D., … Wright, T. J. (2013). Mantle upwelling and initiation of rift segmentation beneath the Afar Depression. *Geology*, *41*(6), 635–638. doi: 10.1130/G33925.1

Hammond, J. O. S., Kendall, J. M., Stuart, G. W., Keir, D., Ebinger, C., Ayele, A., & Belachew, M. (2011). The nature of the crust beneath the Afar triple junction: Evidence from receiver functions. *Geochemistry, Geophysics, Geosystems*, *12*(12). doi: 10.1029/2011GC003738

Hooper, A., Bekaert, D., Spaans, K., & Arıkan, M. (2012). Recent advances in SAR interferometry time series analysis for measuring crustal deformation. *Tectonophysics*, *514*, 1–13.

Hussain, E., Hooper, A., Wright, T. J., Walters, R. J., & Bekaert, D. P. (2016). Interseismic strain accumulation across the central North Anatolian Fault from iteratively unwrapped InSAR measurements. *Journal of Geophysical Research: Solid Earth*, *121*, 9000–9019. doi: 10.1002/2016JB013108

Illsley-Kemp, F., Keir, D., Bull, J. M., Gernon, T. M., Ebinger, C., Ayele, A., ... Belachew, M. (2018). Seismicity during continental breakup in the Red Sea Rift of Northern Afar. *Journal of Geophysical Research: Solid Earth*, *123*, 2345–2362. doi: 10.1002/2017JB014902

Jung, J., Kim, D.-j., & Park, S.-E. (2013). Correction of atmospheric phase screen in time series insar using wrf model for monitoring volcanic activities. *IEEE Transactions on Geoscience and Remote Sensing*, *52*(5), 2678–2689.

Kendall, J. M., Stuart, G. W., Ebinger, C. J., Bastow, I. D., & Keir, D. (2005). Magma-assisted rifting in Ethiopia. *Nature*, *433*(7022), 146–148. doi: 10.1038/nature03161

Kidane, T. (2016). Strong clockwise block rotation of the Ali-Sabieh/Aïsha Block: evidence for opening of the Afar Depression by a saloon-door' mechanism. *Geological Society, London, Special Publications*, *420*, 209–219. doi: 10.1144/SP420.10

King, R., Floyd, M., Reilinger, R., & Bendick, R. (2019). GPS velocity field (MIT 2019.0) for the East African Rift System generated by King et al.. Interdisciplinary Earth Data Alliance (IEDA). *Accessed on 20 Sep 2019*.

Kogan, L., Fisseha, S., Bendick, R., Reilinger, R., McClusky, S., King, R., & Solomon, T. (2012). Lithospheric strength and strain localization in continental extension from observations of the East African Rift. *Journal of Geophysical Research: Solid Earth*, *117*(B03402). doi: 10.1029/2011JB008516

Lanari, R., Casu, F., Manzo, M., Zeni, G., Berardino, P., Manunta, M., & Pepe, A. (2007). An overview of the Small BAseline Subset algorithm: A DInSAR technique for surface deformation analysis. *Pure and Applied Geophysics*, *164*(4), 637–661. doi: 10.1007/s00024-007-0192-9

Lavayssière, A., Rychert, C., Harmon, N., Keir, D., Hammond, J. O., Kendall, J.-M., ... Leroy, S. (2018). Imaging lithospheric discontinuities beneath the Northern East African Rift Using S-to-P receiver functions. *Geochemistry, Geophysics, Geosystems*, *19*(10), 4048–4062.

Lazecky, M., Maghsoudi, Y., Morishita, Y., Wright, T. J., Hooper, A., Elliott, J., ... Spaans, K. (in review.). LiCSAR: An Automated InSAR Tool for Monitoring Tectonic and Volcanic Activity. *Remote Sensing*.

Liu, S., Hanssen, R., Samiei-Esfahany, S., Hooper, A., & Van Leijen, F. (2011). Separating non-linear deformation and atmospheric phase screen (APS) for InSAR time series analysis using least-squares collocation. In *Proceedings of the advances in the science and applications of sar interferometry, esa fringe 2009, workshop esa.*

McClusky, S., Reilinger, R., Ogubazghi, G., Amleson, A., Healeb, B., Vernant, P., ... Kogan, L. (2010). Kinematics of the southern Red Sea-Afar Triple Junction and implications for plate dynamics. *Geophysical Research Letters*, *37*(L05301). doi: 10.1029/2009GL041127

Mogi, K. (1958). Relations between the Eruptions of Various Volcanoes and the Defomormations of the Ground Surfaces around them. *Bulletin of the Earthquake Research Institute*, *36*, 99–134.

Moore, C., Wright, T., Hooper, A., & Biggs, J. (2019). The 2017 eruption of Erta 'Ale volcano, Ethiopia: Insights in the shallow axial plumbing system of an incipient mid-ocean ridge. *Geochemistry, Geophysics, Geosystems*, *20*(12).

Morishita, Y., Lazecky, M., Wright, T. J., Weiss, J. R., Elliott, J. R., & Hooper, A. (2020). LiCSBAS: An Open-Source InSAR Time Series Analysis Package Integrated with the LiCSAR Automated Sentinel-1 InSAR Processor. *Remote Sensing*, *12*(3), 424.

Nobile, A., Pagli, C., Keir, D., Wright, T. J., Ayele, A., Ruch, J., & Acocella, V. (2012). Dike-fault interaction during the 2004 Dallol intrusion at the northern edge of the Erta Ale Ridge (Afar, Ethiopia). *Geophysical Research Letters*, *39*(L19305). doi: 10.1029/2012GL053152

Okada, Y. (1985). Surface deformation due to shear and tensile faults in a half-space. *Bulletin of the seismological society of America*, *75*(4), 1135–1154.

Pagli, C., Wang, H., Wright, T. J., Calais, E., & Lewi, E. (2014). Current plate boundary deformation of the Afar rift from a 3-D velocity field inversion of InSAR and GPS. *Journal of Geophysical Research: Solid Earth*, *119*, 8562–8575. doi: 10.1002/2014JB011391

Pagli, C., Wright, T. J., Ebinger, C. J., Yun, S. H., Cann, J. R., Barnie, T., & Ayele, A. (2012). Shallow axial magma chamber at the slow-spreading Erta Ale Ridge. *Nature Geoscience*, *5*(4), 284–288. doi: 10.1038/ngeo1414

Refice, A., Belmonte, A., Bovenga, F., & Pasquariello, G. (2011). On the use of anisotropic covariance models in estimating atmospheric DInSAR contributions. *IEEE Geoscience and Remote Sensing Letters*, *8*(2), 341–345.

Saria, E., Calais, E., Stamps, D. S., Delvaux, D., & Hartnady, C. J. (2014). Present-day kinematics of the East African Rift. *Journal of Geophysical Research: Solid Earth*, *119*, 3584–3600. doi: 10.1002/2013JB010901

Shen, L., Hooper, A., & Elliott, J. (2019). A Spatially Varying Scaling Method for InSAR Tropospheric Corrections Using a High-Resolution Weather Model. *Journal of Geophysical Research: Solid Earth*, *124*(4), 4051–4068.

Sousa, J. J., Hooper, A. J., Hanssen, R. F., Bastos, L. C., & Ruiz, A. M. (2011). Persistent Scatterer InSAR: A comparison of methodologies based on a model of temporal deformation vs. spatial correlation selection criteria. *Remote Sensing of Environment*, *115*(10), 2652–2663.

Stork, A. L., Stuart, G. W., Henderson, C. M., Keir, D., & Hammond, J. O. (2013). Uppermost mantle (Pn) velocity model for the Afar region, Ethiopia: An insight into rifting processes. *Geophysical Journal International*, *193*, 321–328. doi: 10.1093/gji/ggs106

Tarantola, A., Ruegg, J. C., & Lepine, J. C. (1979). Geodetic evidence for rifting in Afar a brittle-elastic model of the behaviour of the lithosphere. *Earth and Planetary Science Letters*, *45*, 435–444. doi: 10.1016/0012-821X(79)90142-0

Temtime, T., Biggs, J., Lewi, E., Hamling, I., Wright, T., & Ayele, A. (2018). Spatial and temporal patterns of deformation at the Tendaho geothermal prospect, Ethiopia. *Journal of Volcanology and Geothermal Research*, *357*, 56–67. doi: 10.1016/j.jvolgeores.2018.04.004

Tiberi, C., Ebinger, C., Ballu, V., Stuart, G., & Oluma, B. (2005). Inverse models of gravity data from the Red Sea-Aden-East African rifts triple junction zone. *Geophysical Journal International*, *163*, 775–787. doi: 10.1111/j.1365-246X.2005.02736.x

Wang, H., & Wright, T. (2012). Satellite geodetic imaging reveals internal deformation of western Tibet. *Geophysical Research Letters*, *39*(7).

Wang, H., Wright, T. J., Yu, Y., Lin, H., Jiang, L., Li, C., & Qiu, G. (2012). InSAR reveals coastal subsidence in the Pearl River Delta, China. *Geophysical Journal International*, *191*(3), 1119–1128.

Weiss, J. R., Walters, R. J., Morishita, Y., Wright, T. J., Lazecky, M., Wang, H., ... Parsons, B. (2020). High-resolution Surface Velocities and Strain for Anatolia

from Sentinel-1 InSAR and GNSS Data. *EarthArXiv*.
Werner, C., Wegmuller, U., Strozzi, T., & Wiesmann, A. (2000). GAMMA SAR and interferometric processing software. *European Space Agency, (Special Publication) ESA SP*(461), 211–219.
Wiart, P., & Oppenheimer, C. (2000). Largest known historical eruption in Africa: Dubbi volcano, Eritrea, 1861. *Geology*, *28*(4), 291–294. doi: 10.1130/0091-7613(2000)28⟨291:LKHEIA⟩2.0.CO;2
Wolfenden, E., Ebinger, C., Yirgu, G., Deino, A., & Ayalew, D. (2004). Evolution of the northern Main Ethiopian rift: Birth of a triple junction. *Earth and Planetary Science Letters*, *224*(1-2), 213–228. doi: 10.1016/j.epsl.2004.04.022
Wright, T. J., Ebinger, C., Biggs, J., Ayele, A., Yirgu, G., Keir, D., & Stork, A. (2006). Magma-maintained rift segmentation at continental rupture in the 2005 Afar dyking episode. *Nature*, *442*(7100), 291–294. doi: 10.1038/nature04978
Wright, T. J., Parsons, B. E., & Zhong, L. (2004). Toward mapping surface deformation in three dimensions using InSAR. *Geophysical Research Letters*, *31*(L01607). doi: 10.1029/2003GL018827
Wright, T. J., Sigmundsson, F., Pagli, C., Belachew, M., Hamling, I. J., Brandsdóttir, B., … Calais, E. (2012). *Geophysical constraints on the dynamics of spreading centres from rifting episodes on land* (Vol. 5) (No. 4). doi: 10.1038/ngeo1428
Yu, C., Li, Z., & Penna, N. T. (2018). Interferometric synthetic aperture radar atmospheric correction using a GPS-based iterative tropospheric decomposition model. *Remote Sensing of Environment*, *204*, 109–121. doi: 10.1016/j.rse.2017.10.038
Yu, C., Penna, N. T., & Li, Z. (2017). Generation of real-time mode high-resolution water vapor fields from GPS observations. *Journal of Geophysical Research*, *122*(3), 2008–2025. doi: 10.1002/2016JD025753

Supporting Information for "Rift Focussing and Magmatism During Late-Stage Rifting in Afar, Ethiopia"

C. Moore[1], T. Wright[1], A. Hooper[1]

[1]COMET, School of Earth and Environment, University of Leeds, Leeds, LS2 9JT, UK

Contents of this file

Corresponding author: Chris Moore, COMET, School of Earth and Environment, University of Leeds, Leeds, LS2 9JT, UK (ee12cm@leeds.ac.uk)

Time Series Methodology

Our SBAS style and time series methodology from unwrapped interferograms to 3D (rift-perpendicular, rift-parallel, vertical) average velocities consists of the following steps:

1. Invert each pixel for a LOS displacement time series using an SBAS style least-squares inversion as shown in Equation 2 for a network of 5 interferograms (i_{01}, i_{02}, i_{12}, i_{13}, i_{23}) covering 4 epochs (d_0, d_1, d_2, d_3) with zero displacement at the first epoch ($d_0 = 0$). We perform this inversion at each pixel in the frame using all available coherent interferograms, rejecting pixels where the interferogram network at any epoch is disconnected.

$$\begin{bmatrix} i_{01} \\ i_{02} \\ i_{12} \\ i_{13} \\ i_{23} \end{bmatrix} = \begin{bmatrix} 1 & 0 & 0 \\ 0 & 1 & 0 \\ -1 & 1 & 0 \\ -1 & 0 & 1 \\ 0 & -1 & 1 \end{bmatrix} \begin{bmatrix} d_1 & d_2 & d_3 \end{bmatrix} \tag{2}$$

2. Estimate the error in the time series using the RMS misfit.

(i) Filter the displacement time series at each pixel using a Laplacian filter with a temporal width of 3 epochs with a scaling factor (K) of 3 (see Equation 3 for a time series of unfiltered displacements (d_0, d_1, d_2, d_3), filtered displacements (f_0, f_1, f_2, f_3) and the time gaps between epochs (t_{01}, t_{12}, t_{23}).

$$\begin{bmatrix} d_0 \\ d_1 \\ d_2 \\ d_3 \end{bmatrix} = K \begin{bmatrix} 1/K & 0 & 0 & 0 \\ -t_{01} & t_{01} + t_{12} & -t_{12} & 0 \\ 0 & -t_{12} & t_{12} + t_{23} & -t_{23} \\ 0 & 0 & 0 & 1/K \end{bmatrix} \begin{bmatrix} f_0 & f_1 & f_2 & f_3 \end{bmatrix} \tag{3}$$

(ii) For each pixel, we calculate the misfit of the unfiltered time series against the Laplacian filtered time series at every epoch ($m_{xyt} = d_{xyt} - f_{xyt}$).

(iii) Using Equation 4, we calculate the RMS misfit of each pixel (r_{xy}) using the time series of misfits (m_t), and the RMS misfit of each epoch (r_t) using the misfit of every pixel

(m_{xy}).

$$r = \sqrt{\frac{m_1^2 + m_2^2 + ...m_N^2}{N}} \tag{4}$$

(iv) To resolve an RMS misfit value for each pixel at every epoch (r_{xyt}), we scale the spatial RMS misfit map (r_{xy}) to the value of temporal RMS misfit at each epoch (r_t) using the RMS misfit of r_{xy}.

$$r_{xyt} = r_{xy} \frac{r_t}{\sqrt{\frac{r_{11}^2 + r_{12}^2 + r_{21}^2 + ...r_{NM}^2}{NM}}} \tag{5}$$

3. Calculate the APS and remove from the LOS displacement time series.

(i) Low-pass filter the time series of each pixel using a local linear trend with a fixed filter width of $\pm$ 0.5 years from the target epoch. The weighting of the epoch displacements is dependant on the temporal distance from the target epoch, the RMS misfit value, and outlier rejection. By editing the "smooth" function in Matlab, we convert the RMS misfit values into weights using the Bi-Square function (Cleveland & Devlin, 1988), where zero weight is given to RMS values that are $>$ 6 standard deviations of the local misfits.

(ii) Remove the low-pass filtered time series from the unfiltered data to create a high-pass filtered time series.

(iii) On the high-pass temporal filtered data, apply a low-pass spatial filter for each epoch using a Gaussian kernel with a half-width of $\sim$ 2 km to resolve the APS.

(iv) Remove the calculated APS from the displacement time series, and correct for any residual orbital or atmospheric errors by inverting for and removing planar ramps in space, and a linear trend of phase with elevation.

4. Calculate the average LOS velocity for each pixel from the time series of displacements (d_1, d_2, ... d_N, with time steps t_1, t_2, ... t_N) by inverting for the average displacement rate (v) and a constant offset (c, to allow the displacement at $t = 0$ to be non-zero). To resolve uncertainties in the average velocity estimates (Q_{mm}), we include a data VCM (Q_{dd}) by using the time series of RMS misfit values at each pixel (r_1, r_2, ... r_N) as independent error sources (see Equations 6-9).

$$Q_{dd} = \begin{bmatrix} r_1^2 & 0 & ... & 0 \\ 0 & r_2^2 & ... & 0 \\ ... & ... & ... & ... \\ 0 & 0 & ... & r_N^2 \end{bmatrix} \tag{6}$$

$$G = \begin{bmatrix} t_1 & 1 \\ t_2 & 1 \\ ... & ... \\ t_N & 1 \end{bmatrix} \tag{7}$$

$$Q_{mm} = (G^T Q_{dd}^{-1} G)^{-1} \tag{8}$$

$$\begin{bmatrix} v & c \end{bmatrix} = Q_{mm} G^T Q_{dd}^{-1} \begin{bmatrix} d_1 \\ d_2 \\ ... \\ d_N \end{bmatrix} \tag{9}$$

5. Connect the frame LOS velocity maps within their respective tracks.

(i) For each track, we sub-sample the frame velocity maps to 5×5 km in frame overlap regions, and 10×10 km elsewhere.

(ii) Keeping one frame in the track uncorrected, we reference the other frames to it by inverting for planar ramps in space for each frame such that the values in the frame overlap regions are equal. We then remove the ramps from the respective frames, and use the mean value in the frame overlap regions when combining the frames into a single track.

6. Reference the track LOS velocities to a stable Nubia GNSS reference frame.

(i) Convert the GNSS velocities in the east (E) and north (N) directions to rift-perpendicular ($H1$) and rift-parallel ($H2$) directions using Equation 10, using the orientation of the rift axis (α) of 151°N. Then interpolate smooth GNSS velocity fields in the rift-perpendicular and rift-parallel directions using the natural neighbour algorithm and the "griddata" function in Matlab.

$$\begin{bmatrix} E \\ N \end{bmatrix} = \begin{bmatrix} cos(\alpha) & -sin(\alpha) \\ sin(\alpha) & -cos(\alpha) \end{bmatrix} \begin{bmatrix} H1 & H2 \end{bmatrix} \tag{10}$$

(ii) After masking areas with surface deformation that is not related to the long-wavelength plate spreading (i.e. related to volcanic or anthropogenic activity), we sub-sample the track velocities to 5×5 km in track overlap regions, and 10×10 km elsewhere.

(iii) Using the points where there are ascending, descending, and interpolated GNSS data, we invert for 3D velocities (rift-perpendicular, rift-parallel, vertical, see Equation 1 (main text)) and a quadratic function for each track. We then remove the quadratic function from each track to resolve LOS velocities referenced to stable Nubia.

7. Resolve 3D velocities (rift-perpendicular, rift-parallel, vertical) at each pixel (see Equation 1 (main text)), using the smooth GNSS rift-parallel velocity field to help constrain the inversion (e.g. Weiss et al., 2020), and uncertainties in LOS velocity as independent errors in a VCM (as shown in Equation 6).

References

Bagnardi, M., & Hooper, A. (2018). Inversion of Surface Deformation Data for Rapid Estimates of Source Parameters and Uncertainties: A Bayesian Approach. *Geochemistry, Geophysics, Geosystems*, *19*. doi: 10.1029/2018GC007585

Cleveland, W. S., & Devlin, S. J. (1988). Locally weighted regression: an approach to regression analysis by local fitting. *Journal of the American statistical association*, *83*(403), 596–610.

King, R., Floyd, M., Reilinger, R., & Bendick, R. (2019). GPS velocity field (MIT 2019.0) for the East African Rift System generated by King et al.. Interdisciplinary Earth Data Alliance (IEDA). *Accessed on 20 Sep 2019*.

Mogi, K. (1958). Relations between the Eruptions of Various Volcanoes and the Defomormations of the Ground Surfaces around them. *Bulletin of the Earthquake Research Institute*, *36*, 99–134.

Okada, Y. (1985). Surface deformation due to shear and tensile faults in a half-space. *Bulletin of the seismological society of America*, *75*(4), 1135–1154.

Weiss, J. R., Walters, R. J., Morishita, Y., Wright, T. J., Lazecky, M., Wang, H., ... Parsons, B. (2020). High-resolution Surface Velocities and Strain for Anatolia from Sentinel-1 InSAR and GNSS Data. *EarthArXiv*.

Yu, C., Li, Z., & Penna, N. T. (2018). Interferometric synthetic aperture radar atmospheric correction using a GPS-based iterative tropospheric decomposition model. *Remote Sensing of Environment*, *204*, 109–121. doi: 10.1016/j.rse.2017.10.038

Yu, C., Penna, N. T., & Li, Z. (2017). Generation of real-time mode high-resolution water vapor fields from GPS observations. *Journal of Geophysical Research*, *122*(3), 2008–2025. doi: 10.1002/2016JD025753

Frame	Start Date	End Date	No. of IFGs
006D-07728-131313	11.11.2014	30.06.2019	198
006D-07929-131313	18.10.2014	17.08.2019	334
014A-07524-101303	23.11.2014	24.02.2019	85
014A-07688-131313	23.11.2014	18.07.2019	223
014A-07885-131313	30.10.2014	18.07.2019	187
079D-07503-061113	23.11.2015	10.08.2019	178
079D-07694-131313	23.10.2014	17.07.2019	337
079D-07894-131313	23.10.2014	17.07.2019	277
087A-07674-131313	11.10.2014	11.03.2017	92
087A-07889-131313	11.10.2014	11.03.2017	82
116A-07590-071313	13.10.2014	13.07.2019	316
116A-07768-131305	12.12.2014	13.07.2019	193

Table S1. Start date, end date (DD.MM.YYYY), and the number of interferograms (IFGs) used to build the displacement time series for each frame. Frame names are defined by the track (e.g. 006D for descending track 6), the frame ID (e.g. 07728), and the number of bursts in each of the 3 sub-swaths within the frame (e.g. 131313 for a maximum of 13 bursts in each sub-swath).

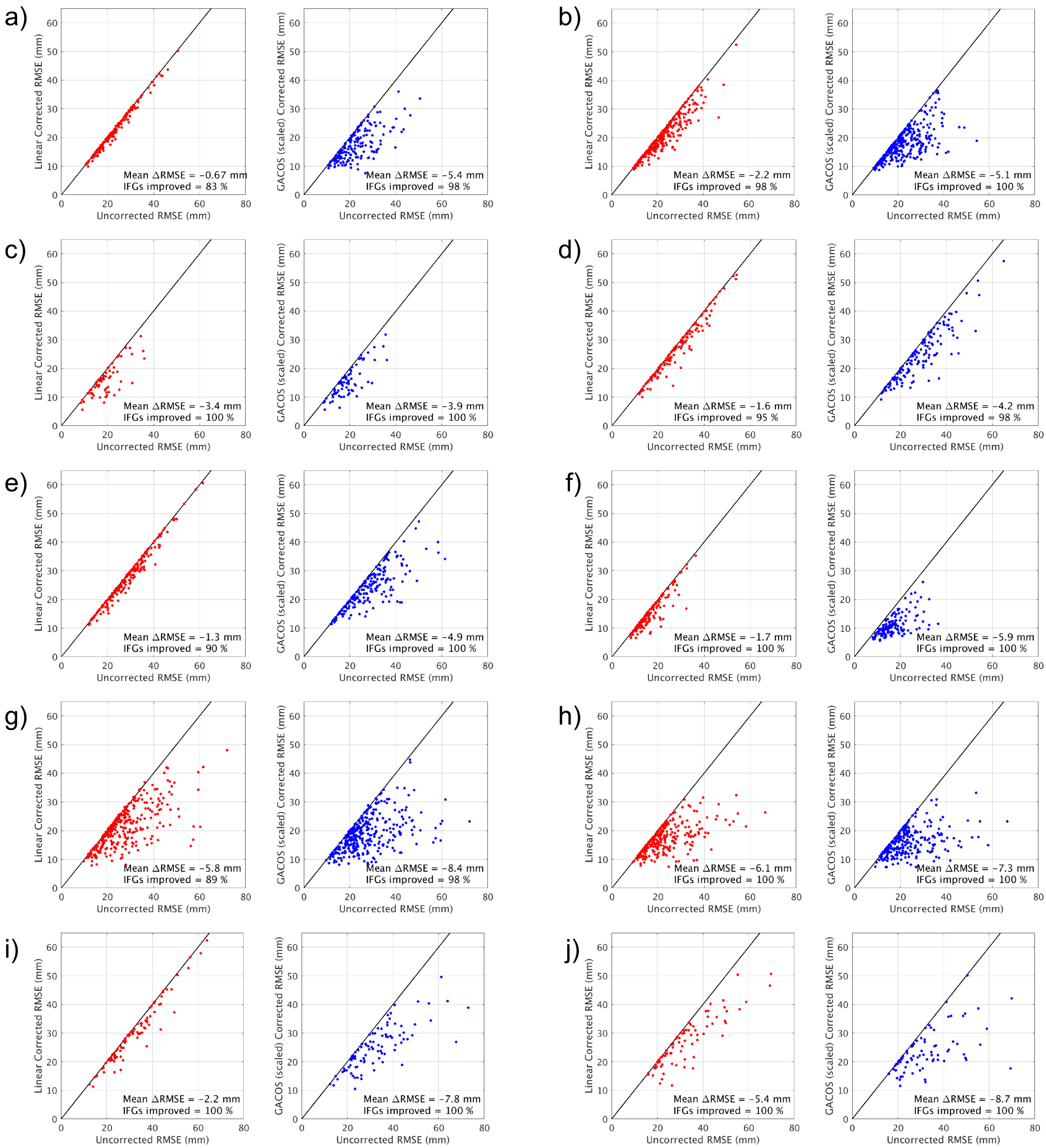
a)
Linear Corrected RMSE (mm)
Uncorrected RMSE (mm)
Mean ΔRMSE = −0.67 mm
IFGs improved = 83 %
GACOS (scaled) Corrected RMSE (mm)
Mean ΔRMSE = −5.4 mm
IFGs improved = 98 %
b)
Mean ΔRMSE = −2.2 mm
IFGs improved = 98 %
Mean ΔRMSE = −5.1 mm
IFGs improved = 100 %
c)
Mean ΔRMSE = −3.4 mm
IFGs improved = 100 %
Mean ΔRMSE = −3.9 mm
IFGs improved = 100 %
d)
Mean ΔRMSE = −1.6 mm
IFGs improved = 95 %
Mean ΔRMSE = −4.2 mm
IFGs improved = 98 %
e)
Mean ΔRMSE = −1.3 mm
IFGs improved = 90 %
Mean ΔRMSE = −4.9 mm
IFGs improved = 100 %
f)
Mean ΔRMSE = −1.7 mm
IFGs improved = 100 %
Mean ΔRMSE = −5.9 mm
IFGs improved = 100 %
g)
Mean ΔRMSE = −5.8 mm
IFGs improved = 89 %
Mean ΔRMSE = −8.4 mm
IFGs improved = 98 %
h)
Mean ΔRMSE = −6.1 mm
IFGs improved = 100 %
Mean ΔRMSE = −7.3 mm
IFGs improved = 100 %
i)
Mean ΔRMSE = −2.2 mm
IFGs improved = 100 %
Mean ΔRMSE = −7.8 mm
IFGs improved = 100 %
j)
Mean ΔRMSE = −5.4 mm
IFGs improved = 100 %
Mean ΔRMSE = −8.7 mm
IFGs improved = 100 %

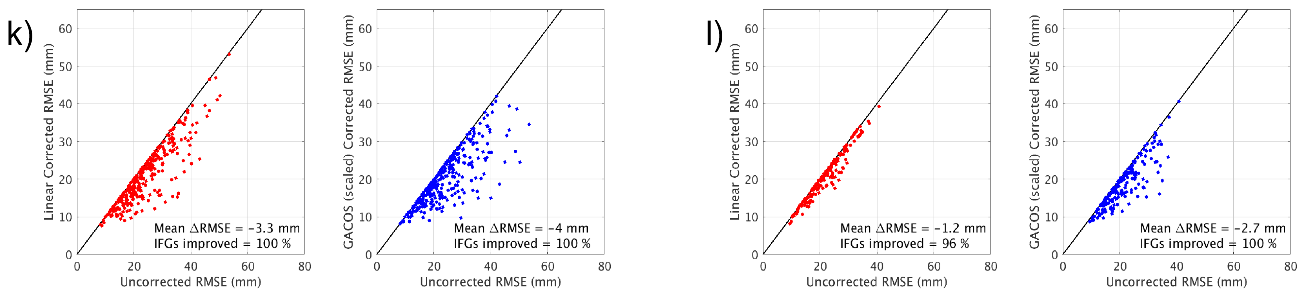

Figure S1. Residual root-mean-square error (RMSE) for all interferograms in each frame after applying atmospheric phase delay corrections using a linear correlation of phase with elevation (red), and a scaled GACOS atmospheric model (blue) (Yu et al., 2017, 2018). Also shown is the mean change in RMSE, and the percentage of interferograms where the RMSE was improved following the correction. Frames: (a) 006D-07728-131313, (b) 006D-07929-131313, (c) 014A-07524-101303, (d) 014A-07688-131313, (e) 014A-07885-131313, (f) 079D-07503-061113, (g) 079D-07694-131313, (h) 079D-07894-131313, (i) 087A-07674-131313, (j) 087A-07889-131313, (k) 116A-07590-071313, (l) 116A-07768-131305.

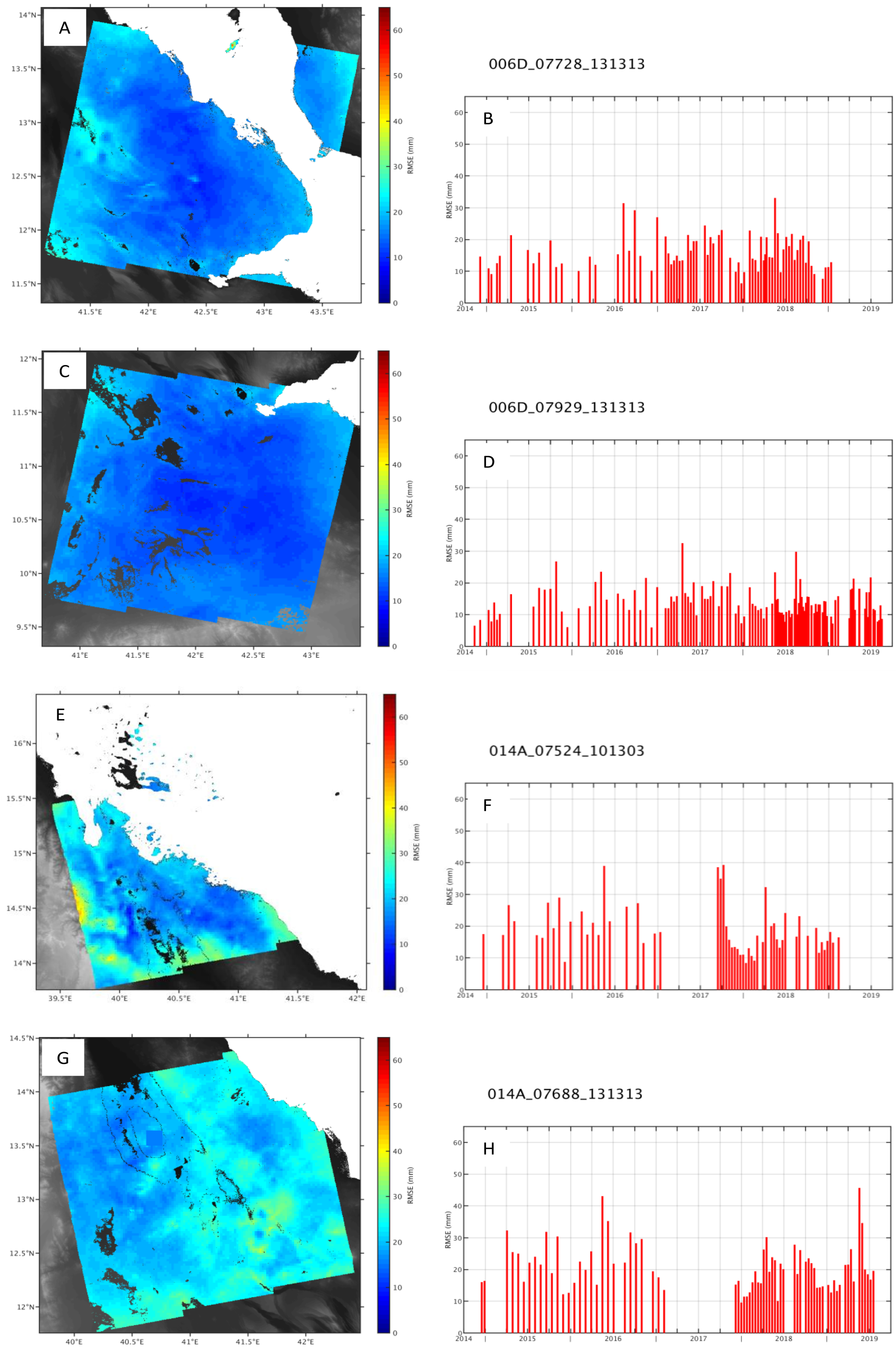
A
006D_07728_131313
B
C
006D_07929_131313
D
E
014A_07524_101303
F
G
014A_07688_131313
H
RMSE (mm)

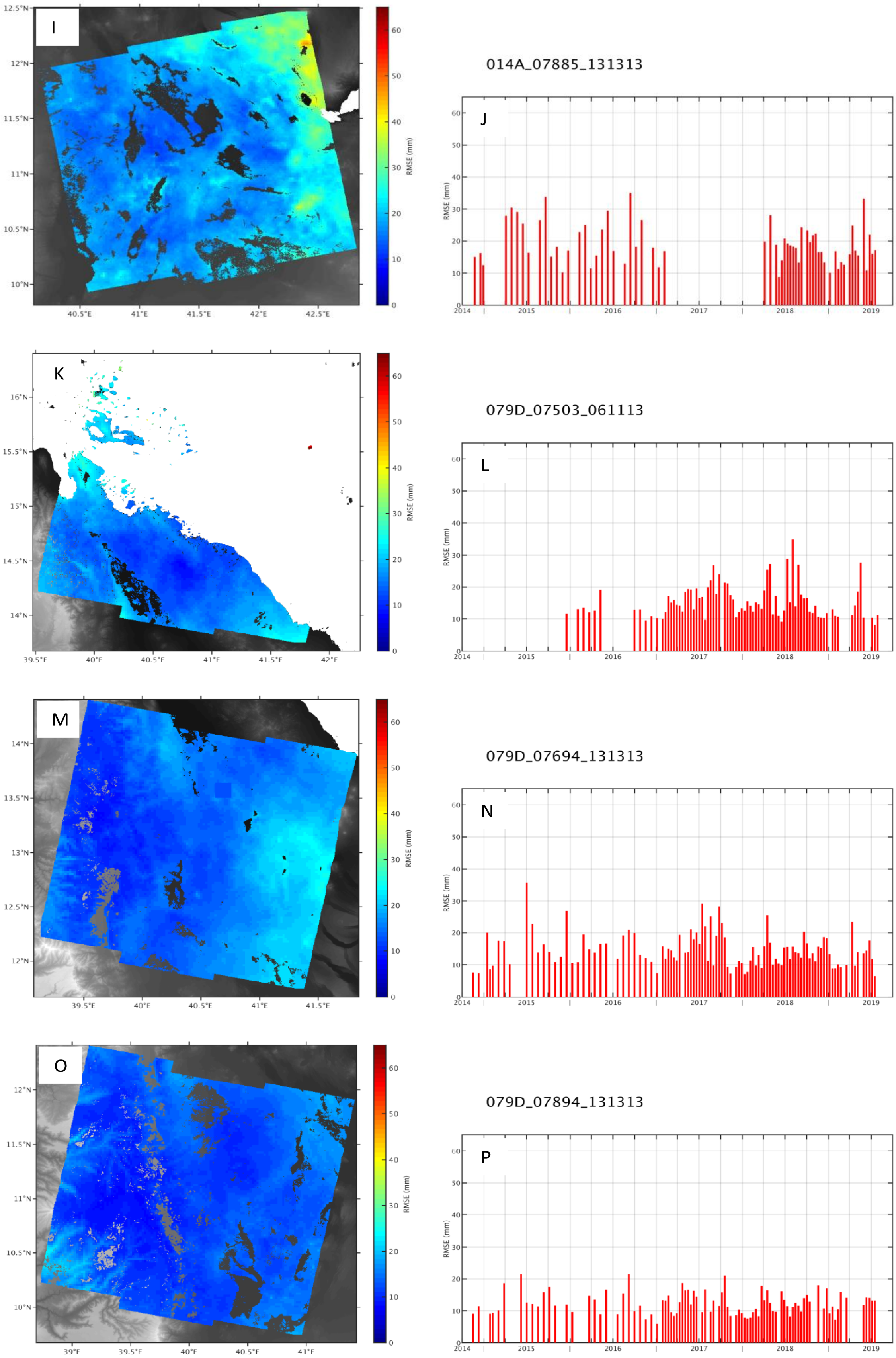

I
J
014A_07885_131313
K
L
079D_07503_061113
M
N
079D_07694_131313
O
P
079D_07894_131313
RMSE (mm)
2014
2015
2016
2017
2018
2019

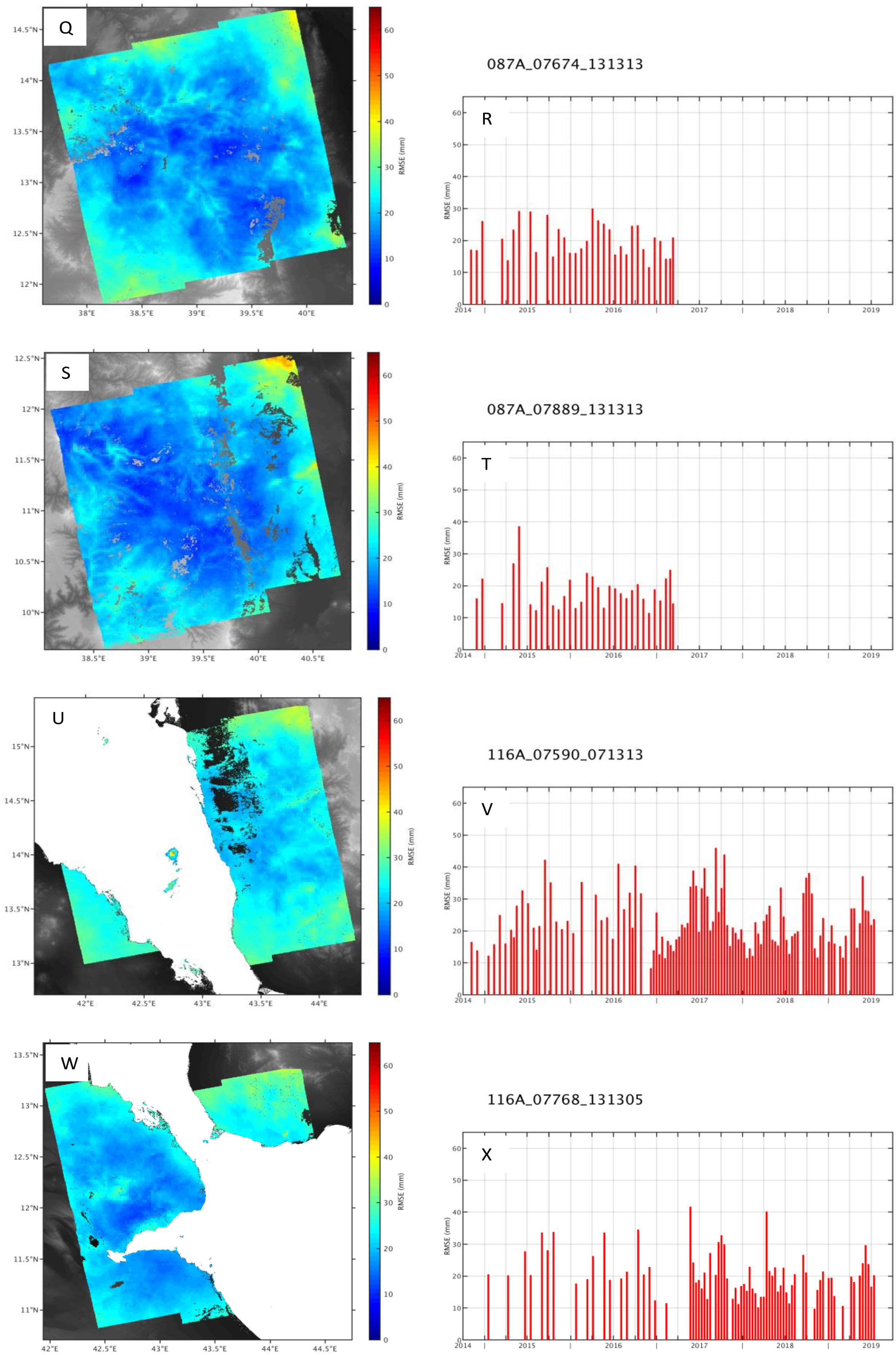
Q
087A_07674_131313
R
S
087A_07889_131313
T
U
116A_07590_071313
V
W
116A_07768_131305
X
RMSE (mm)
2014
2015
2016
2017
2018
2019

Figure S2. Frame root-mean-square error (RMSE) in space for each pixel (A,C,E,G,I,K,M,O,Q,S,U,W) and time for each epoch (B,D,F,H,J,L,N,P,R,T,V,X). Frames: (A,B) 006D-07728-131313, (C,D) 006D-07929-131313, (E,F) 014A-07524-101303, (G,H) 014A-07688-131313, (I,J) 014A-07885-131313, (K,L) 079D-07503-061113, (M,N) 079D-07694-131313, (O,P) 079D-07894-131313, (Q,R) 087A-07674-131313, (S,T) 087A-07889-131313, (U,V) 116A-07590-071313, (W,X) 116A-07768-131305.

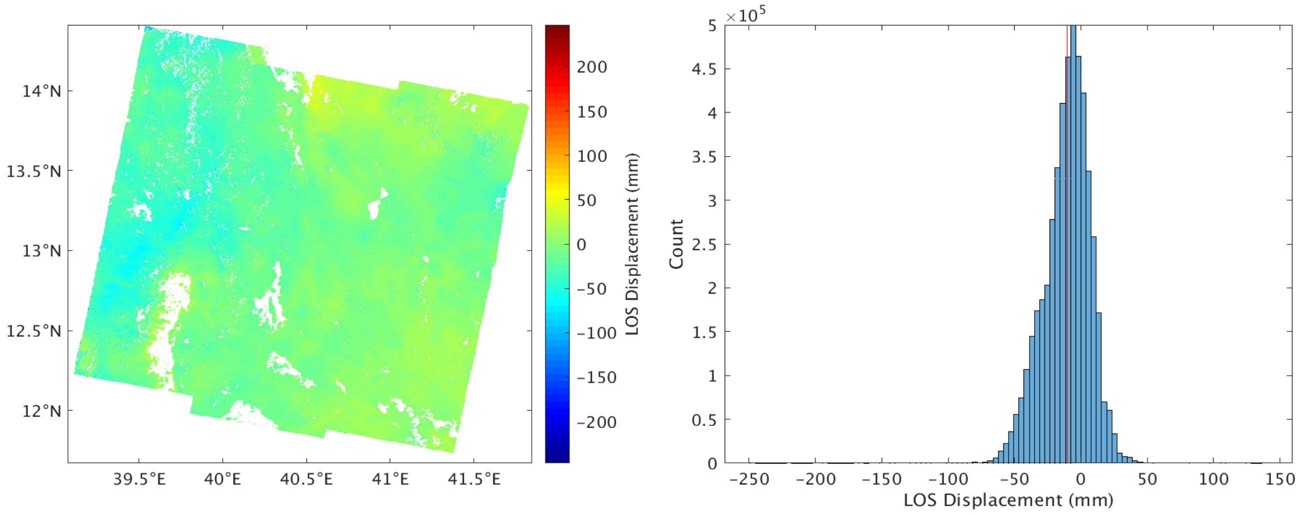

Figure S3. Demonstrating line of sight (LOS) displacement bias ('phase bias') from the difference between 12 and 24 day interferogram 'daisy-chain' stacks for frame 079D-07694-131313 between 06 December 2017 and 11 February 2019. Residuals shown in map view and as a histogram with the mean value indicated by a vertical red line.

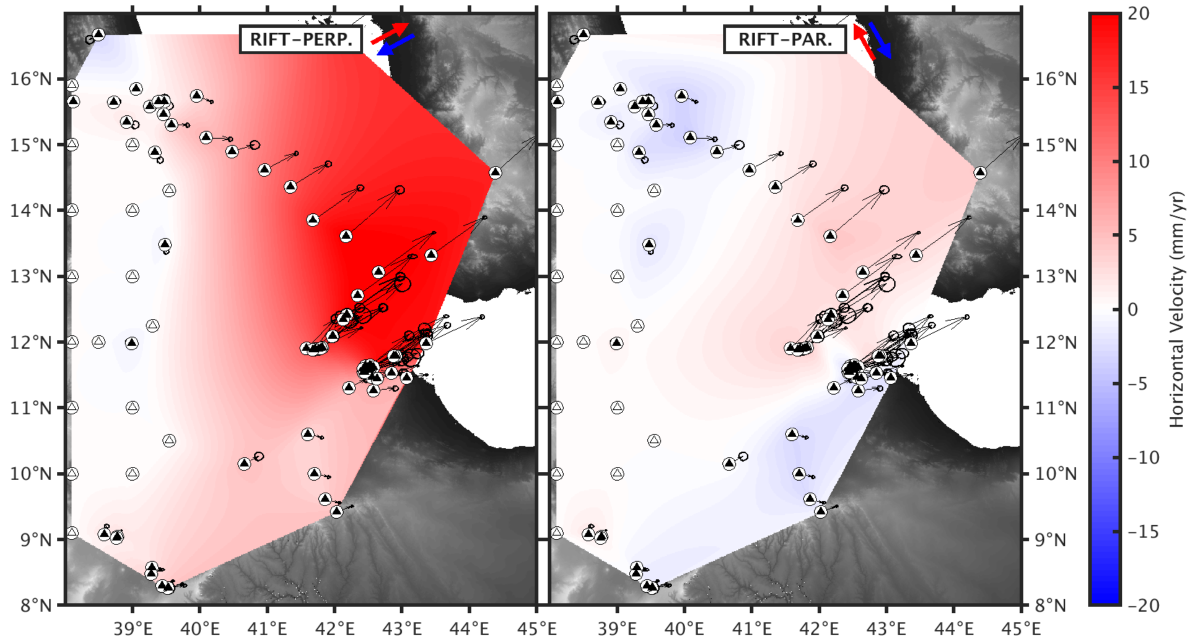

Figure S4. GNSS derived rift-perpendicular (positive towards 61°N) and rift-parallel (positive towards -29°N) horizontal velocity fields. Black triangles indicate the subset of GNSS stations used from (King et al., 2019) with velocity vectors and error ellipses White triangles indicate the synthetic stations with zero velocity on the stable Nubian plate used to help constrain the velocity fields.

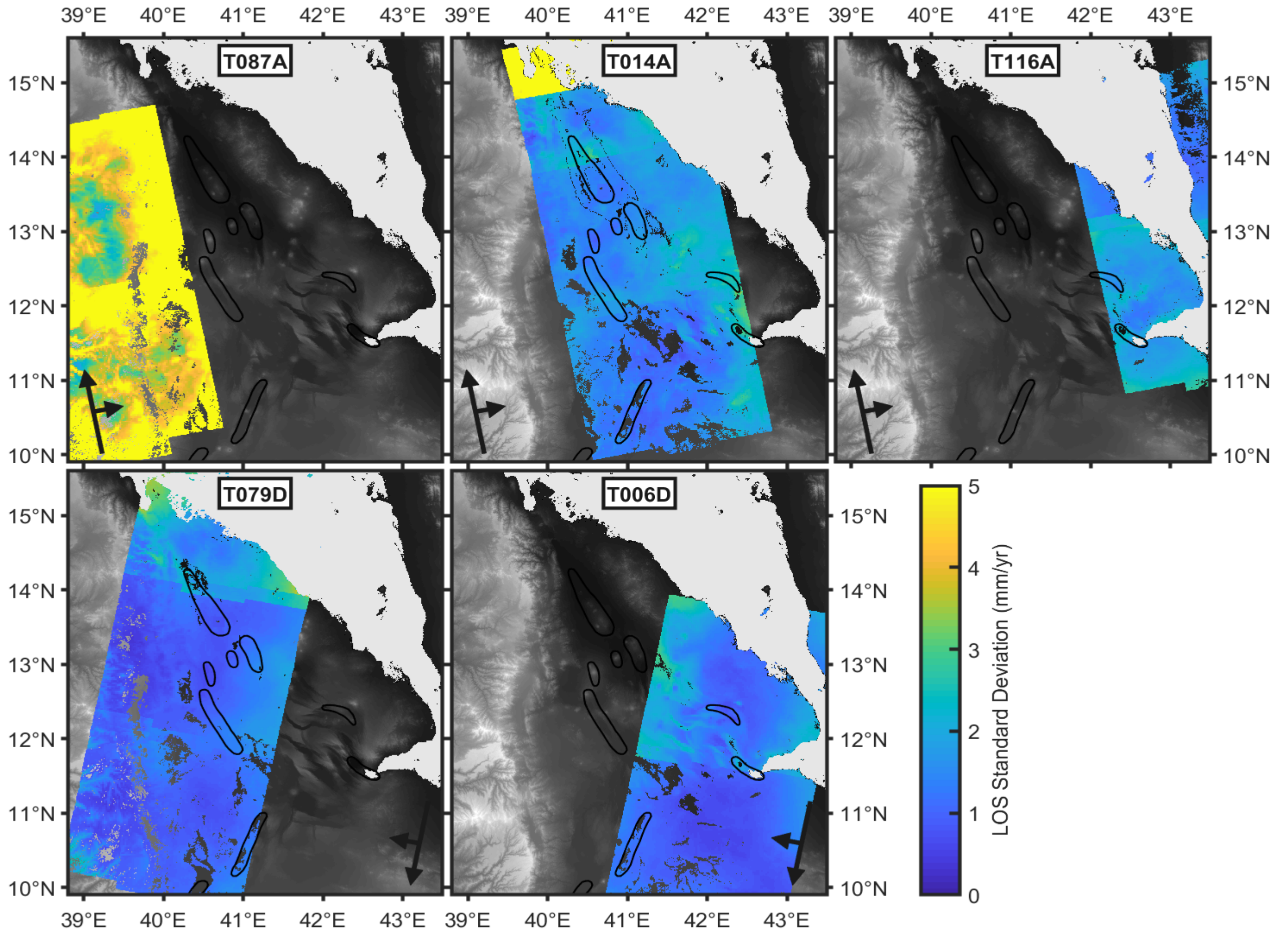

Figure S5. LOS standard deviation over the Afar region between November 2014 and August 2019 from Sentinel-1 tracks T087A, T014A, T116A, T079D, and T006D. Colour scale is limited to 5 mm to highlight variation in regions of low variance. Maximum standard deviation for each track is (2 s.f.): 15 mm/yr (T087A), 13 mm/yr (T014A), 3.2 mm/yr (T116A), 3.8 mm/yr (T079D), 3.1 mm/yr (T006D).

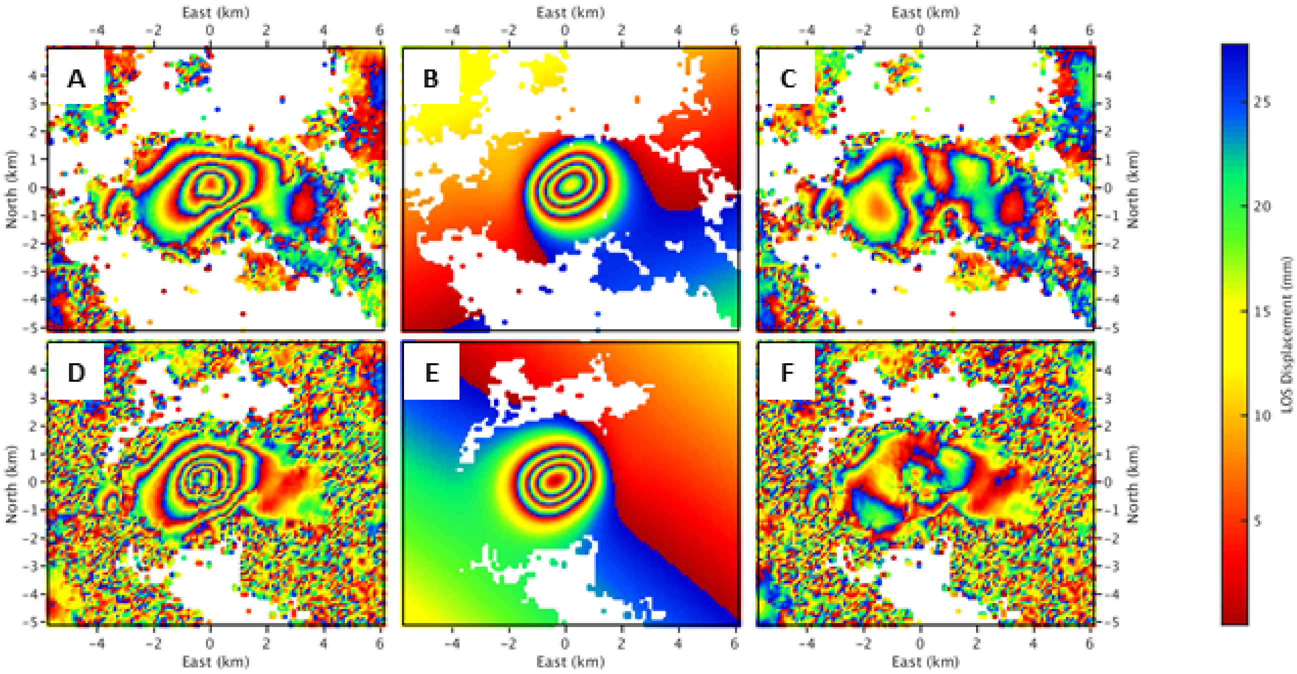

Figure S6. Sentinel-1 data (A,D), GBIS (Bagnardi & Hooper, 2018) model (B,E), and residual (C,F), for 2015-19 surface deformation observed using tracks T079D (A,B,C), and T014A (D,E,F) at Dallol volcano. Surface displacements are shown wrapped where each fringe (red-blue) represents 26 mm of motion towards the satellite in the line of sight. The model consists of a $\sim 1{\times}2$ km horizontal sill (Okada, 1985) at 0.9-1.3 km depth with ~ 0.27 m of contraction. The coordinate system is relative to the centre of the Dallol edifice.

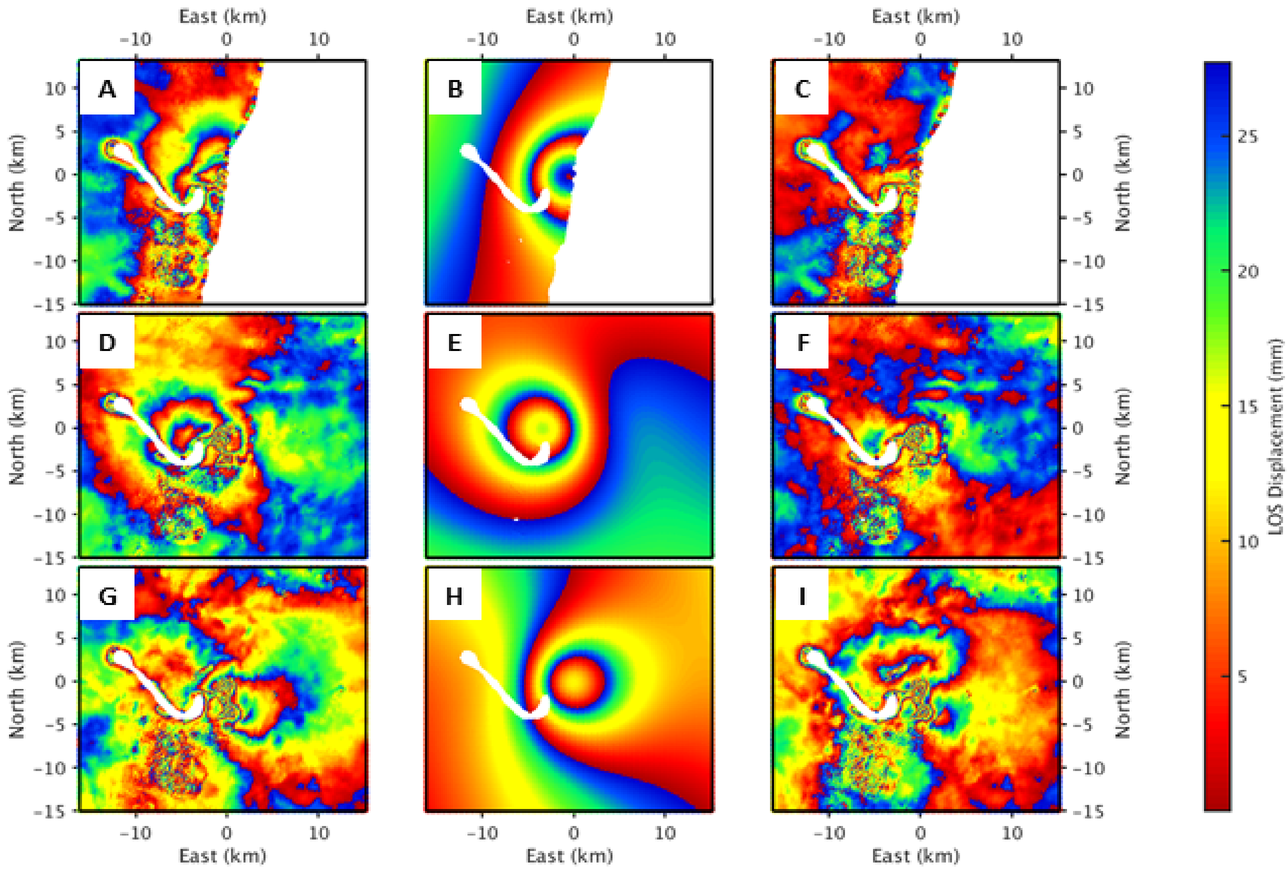

Figure S7. Sentinel-1 data (A,D,G), GBIS (Bagnardi & Hooper, 2018) model (B,E,H), and residual (C,F,I), for 2014-19 surface deformation observed using tracks T079D (A,B,C), T014A (D,E,F), and T006D (G,H,I) at Nabro volcano. Surface displacements are shown wrapped where each fringe (red-blue) represents 26 mm of motion towards the satellite in the line of sight. The model consists of a point source (Mogi, 1958) at 5.5-6.8 km depth with an equivalent volume change of 7-11$\times10^6$ m^3. The coordinate system is relative to the centre of the Nabro edifice.